JGR Oceans

RESEARCH ARTICLE
10.1029/2021JC018381

Wind Effects on Small-Scale River and Creek Plumes

N. B. Basdurak[1,2] and **J. L. Largier**[3,4]

[1]Institute of Marine Sciences, Middle East Technical University, Erdemli/Mersin, Turkey, [2]Leibniz Institute for Baltic Sea Research Warnemünde, Rostock, Germany, [3]Coastal & Marine Sciences Institute, University of California Davis, Bodega Bay, CA, USA, [4]Department of Environmental Science & Policy, University of California Davis, Davis, CA, USA

Key Points:

- Plume bends downwind, with upstream boundary deflected by ambient current and downstream boundary deflected by surface wind stress
- Asymmetry in plume shape between weak upwelling versus downwelling winds vanishes with strong winds that retain the plume nearshore where Ekman transport negligible
- Inertia & buoyancy control the near-field; wind forcing & buoyancy control the mid-field; wind mixing & passive advection control the far-field

Correspondence to:

N. B. Basdurak,
berkay@ims.metu.edu.tr;
berkay.basdurak@io-warnemuende.de

Citation:

Basdurak, N. B., & Largier, J. L. (2023). Wind effects on small-scale river and creek plumes. *Journal of Geophysical Research: Oceans*, *128*, e2021JC018381. https://doi.org/10.1029/2021JC018381

Received 4 JAN 2022
Accepted 20 NOV 2022
Corrected 4 JAN 2023

This article was corrected on 4 JAN 2023. See the end of the full text for details.

Abstract In contrast to large river plumes, Coriolis effects are weak, and inertia is quickly depleted so that the fate and structure of small-scale plumes are more sensitive to tide and wind. Advected alongshore by reversing tidal currents in absence of wind forcing, small buoyant plumes are persistently deflected downwind in presence of alongshore winds and exhibit little tidal variability. The effect of different upwelling/downwelling winds on buoyant outflows ~10 $m^3\ s^{-1}$ is explored. With increasing wind, tidal variability decreases, as does asymmetry in plume characteristics—for strong winds upwelling/downwelling plume structure is similar as the plume is retained closer to the shore. Wind forcing is exerted directly by wind stress on the surface of the plume and indirectly by wind-driven currents that deflect the upwind boundary of the plume. While inertia and buoyancy dominate the inner plume, and wind dominates the outer plume, the mid-plume responds to an interaction of wind and buoyancy forcing that can be indexed by a Plume Wedderburn Number W_{pl} (wind stress vs. density gradients): for weaker winds ($W_{pl} < 1$) surface stress enhances stratification through straining, lengthening the reach of low-salinity waters, whereas for stronger winds ($W_{pl} > 1$) surface stress mixes the plume vertically, shortening the reach of low-salinity waters. However, dilute plume waters extend furthest in strong winds, passively advected several kilometers downwind. Shoreline exposure to outflow transitions from a quasi-symmetrical tide-averaged zone of impact under zero-wind to a heavily skewed zone with persistent weak wind and a one-sided zone for strong wind.

Plain Language Summary Compared to large river plumes, outflow from small rivers and mountainous streams is more sensitive to tides and winds because of the weak Coriolis effect and quickly reduced inertia. Alongshore (upwelling/downwelling) winds carry these small plumes in their direction. We use a numerical model to study the effect of these upwelling/downwelling winds on plumes spreading from small rivers with discharge rates of 10 $m^3\ s^{-1}$ or less. Increasing wind reduces tidal fluctuations in plume patterns such that with strong winds the plume spreads similarly for upwelling and downwelling winds as it remains close to the shore. Wind affects the plume surface directly and the upwind-plume boundary indirectly via wind-driven currents. Inertia and buoyancy control the inner plume while wind and buoyancy control the mid-plume and wind controls the outer plume. Weaker winds increase the plume length and layering by horizontally tilting the density gradients. Stronger winds shorten the plume by vertically mixing it. However, dilute plume waters extend furthest in strong winds, passively advected several kilometers downwind.

1. Introduction

The fate of a small-scale river plume depends largely on the strength of the outflow, which determines how far offshore it extends and therefore what coastal forcing it encounters (e.g., winds, waves, tidal currents, shelf currents). Breaking waves may counteract offshore momentum and trap the small-scale buoyant outflow in the surf zone where it is advected passively alongshore in the surf zone (Rodriguez et al., 2018). Further, the wave-driven longshore current in the surf zone may contribute to trapping river outflow within the surf zone when the cross-flow length scale of the river discharge is smaller than the surf zone width (Wong et al., 2013). However, tidal variability may allow river water to escape the surf zone (Kastner et al., 2019). In the absence of waves, or beyond the surf zone, tidal currents or winds may control the inner shelf dynamics and the direction of the plume propagation. In addition to direct forcing via wind stress on the plume surface, alongshore wind-driven currents can deflect the small-scale river plume. Where Coriolis effects are important, alongshore wind can also force cross-shore responses. Moreover, winds induce local stirring and straining that can weaken or strengthen stratification of the plume layer.

The vast majority of wind-influenced plume studies have focused on large river systems. Observational and numerical studies have shown that large plume characteristics vary in response to changes in the alongshore wind stress and direction (Fong and Geyer, 2001, 2002; Kastner et al., 2018; Kirincich et al., 2005, 2009; Lentz & Largier, 2006; Moffat & Lentz, 2012; Pimenta & Kirwan, 2014; Rennie et al., 1999). Downwelling winds generate significant deepening, surface narrowing, and increased along-shelf transport, with tight attachment to the shore (Moffat & Lentz, 2012). During upwelling winds, however, the plume broadens and may separate from the shore as well as thin enough to break up (Lentz & Largier, 2006). In upwelling regions with strong wind-driven alongshore currents, plumes may be deflected counter to Coriolis deflection and remain detached from the shore owing to active wind-driven upwelling, even for moderate/large outflow rates (Geyer et al., 2000; Kirincich et al., 2005; Pullen & Allen, 2000).

The fate of small-scale river plumes differs significantly from prototypical large plumes due to the lack of a bulge region where rotational forces dictate the plume dynamics. In the absence of significant wave and wind forcing, tidal plumes form. Basdurak et al. (2020) identified three dynamically distinct zones (inertia-driven near-field, buoyancy-driven mid-field, advective far-field) and related these to levels of dilution and freshwater concentration. With wind forcing, these dynamical zones are different.

A recent observational study has shown that the offshore transport of a small-scale buoyant outflow is not governed by Ekman dynamics, but it is instead driven by inertia, wind mixing, and morphology (Tilburg et al., 2011). Also, through remote sensing of plumes in the non-tidal Black Sea, Osadchiev and Sedakov (2019) show asymmetry in plume spreading, contrasting the response to upwelling versus downwelling winds—and formation of a mini-bulge for weak winds and in the absence of tides. We expect that wind forcing often dominates tidal forcing and is the primary determinant of plume trajectory, structure and shore contact where outflow rates are small (i.e., not controlled by buoyancy-Coriolis interaction) and the river mouth is not subject to significant wave forcing. Here we explore the effect of wind strength and direction on small-scale plumes, focusing on alongshore winds which tend to be strong and prevalent along mountainous coasts characterized by small watersheds (e.g., California, Chile, Italy, Portugal, South Africa, Spain, and Turkey). While waves can be significant at times, there are other times when waves are small and many places that are locally or regionally sheltered from waves.

To resolve small-scale plume dynamics and structure in response to alongshore wind forcing, we implement a high-resolution idealized numerical model, building on prior work (Basdurak et al., 2020). With the high-resolution model we can resolve fine scales of the problem, and do so for a number of scenarios with different outflow rates and alongshore wind stress. We use the model to explore the structure and spatiotemporal variability of a small plume subject to upwelling and downwelling winds and tidal currents in the coastal ocean. The model allows us to identify wind-induced effects in small-river plumes, associated inner shelf dynamics and nearshore retention processes.

The aims of this study are: (a) to identify the dynamical response of small-scale river plumes to different strengths of wind forcing, both upwelling and downwelling; (b) to explore when wind enhances plume propagation by straining and when it suppresses it by mixing; (c) to address the effect of wind forcing on plume extent and the extent to which plumes waters are in contact with the shore, that is, "shore contact"; and (d) to analyze the relative importance of wind and tidal forcing on plume characteristics. In Section 3.1 we address the influence of wind on the horizontal structure of the plume, whereas in Section 3.2 we address the vertical structure and plume stratification. Dimensionless numbers are introduced in Section 3.3 and in Sections 3.4 we address the spatial extent of the plume and shore contact, with attention to how it is modulated by both wind forcing and outflow rate.

2. Materials and Methods

2.1. Model Setup

The Regional Ocean Modeling System (ROMS; Rutgers University, version 3.1) was used to investigate the effects of winds on a small-scale buoyant outflow in an idealized coastal domain. The numerical domain was 20 × 5 km in alongshore and cross-shore directions consisting of a uniformly sloping shelf and a 2-m deep, 160-m long, and 15-m wide estuary (Figure 1a). The bathymetry slopes linearly to a maximum depth of 50 m at the offshore boundary, deep enough to allow distinct surface and bottom Ekman layers to develop when wind forcing applied. Grid mesh was denser near the mouth of the estuary and along the coast with spatial resolution: 5–60 m in the cross-shore and 5–80 m alongshore. The model had 10 vertical layers, with finer resolution

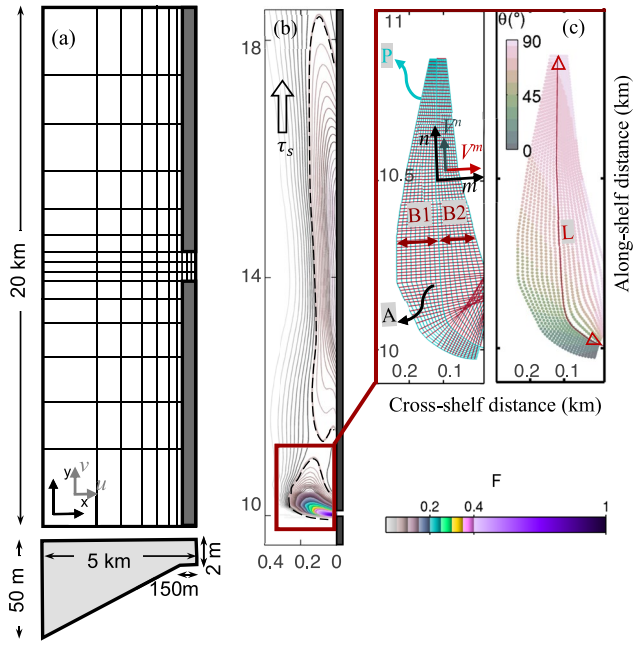

Figure 1. (a) Sketch of the model domain: surface grid, and cross-section. (b) A snapshot of plume-water fraction F at the surface under strong downwelling winds $\tau = 0.5$ Pa during high tide; a threshold value of $F = 0.05$ (black dashed lines) delineates the active plume (contiguous to mouth) from the relict plume (detached from active plume). (c) Right panel: orientation angle with respect to the channel mouth for example, perpendicular to the mouth $\theta = 0°$, or parallel to the shelf $\theta = 90°$; the curvilinear lines shown are interpolated between the plume centerline and the plume boundary on each side of the centerline. Left panel: plume mesh with the curvilinear m–n coordinate system (m cross-plume; n down-plume) used for transformation of the cartesian vector field (u, v) to a curvilinear vector field (V^m, V^n).

near the surface (detailed in Basdurak et al., 2020). Spatially uniform wind forcing of different magnitudes and directions was imposed to explore the response of a small-scale river plume under upwelling and downwelling conditions. A freshwater flux of 10 m^3 s^{-1} ramped up over 3 hr was applied at the head of the estuary (varied in later runs). Tidal forcing was introduced at the boundaries, as a semi-diurnal fluctuation in water surface elevation with a range of 2 m and with the northern boundary phase lagged by 10° from the southern boundary of the domain and interpolated along the western edge. The model was run for 2 days with a time step of $\Delta t = 1$ s. The model spin-up time is less than a day and we analyze data from the second day (longer runs produce repetitive patterns). Results are presented in hours relative to the time of low tide. The model setup was detailed in Basdurak et al. (2020).

2.2. Methodology

The analysis of model results employs the concepts of "outflow fraction" and "plume centerline" (Basdurak et al., 2020). The outflow fraction at any given location is defined as $F = (S_0 - S)/(S_0 - S_m)$, with S_0, S_m and S denoting the salinity of the ambient water, salinity at the mouth and salinity at the point of interest, respectively; using F instead of salinity allows for comparison of tracer fields between outflows of different salinity and density (Figure 1b). The plume centerline (axis of minimum-salinity) follows the zero cross-plume salinity gradient. This method involves finding the geometric centerline of individual polygons bounded by various outflow fractions ranging from 0.05 to 0.45 at intervals of 0.05 (Basdurak et al., 2020).

A right-handed Cartesian coordinate system was used with the x-axis directed toward the coast, y-axis alongshore (positive upcoast) and z-axis vertical (positive up). Upcoast and downcoast refer respectively to locations and orientations to the right and left of the mouth looking offshore (i.e., upcoast is in the direction of Kelvin wave propagation in northern hemisphere). The cross-shore u (positive onshore), alongshore v and vertical w components of velocity are in the x, y and z directions, respectively (Figure 1a). ROMS diagnostics were used to compute the plume dynamics and characteristics, then transformed from the x–y Cartesian coordinates into a curvilinear m–n coordinate system, with n oriented along the centerline (positive outward) and m perpendicular (positive to right of outward)—see Figure 1c (left panel). This transformation requires a rotation that varies spatially and varies over time, based on the local orientation of the centerline.

2.2.1. Plume Shape and Orientation

The horizontal boundaries of the plume are determined by the outflow fraction $F = 0.05$ and along/cross-shore plume extent is calculated from this. We distinguish active plume patches from relict plume patches, identifying active patches as those connected with the estuary mouth (i.e., active outflow) whereas relict patches are local minima that have been disconnected from the active plume and estuary mouth (i.e., a higher salinity saddle point separates active and relict plume patches (Figure 1b).

Plume characteristics and propagation are determined along the plume centerline of the active plume. The orientation of the plume centerline is relative to the orientation of the mouth channel. Positive/negative angles mark the up/down–coast deflection with ±90° denoting shore-parallel propagation and 0° denoting shore-normal propagation (Figure 1c, right panel). Additionally, width-averaged plume characteristics and cross-plume gradients are determined on lines interpolated between the plume boundary and the centerline (Figure 1c, right panel). Because the centerlines are not parallel to the boundaries, the cross-plume gradient calculations are made on another grid (Figure 1c, left panel; red grid, where the grid points are along the transects perpendicular to the centerline). The cross-plume gradients are then interpolated back to the original grid (Figure 1c, right

panel). Lagrangian studies such as McCabe et al. (2008), Kakoulaki et al. (2014), and Kastner et al. (2018) consider cross-plume gradients between water parcels that all left the mouth at the same time. Our approach differs from these studies because we consider the variability in advection between the center and edge of the plume.

The elevation of the interface at the base of the plume z_p is determined by the depth where the local vertical density gradient $\partial_z \rho$ is maximum (and exceeds a 0.05 kg m^{-4} threshold). The plume thickness is defined as $H_P = \eta - z_p$ where η is the elevation of the free surface (Figure A1, left panel; Appendix A1 and A2). Surface geometry of the active plume patches are characterized by plume complexity calculated as the ratio of squared boundary perimeter to the plume surface area P^2/A, plume asymmetry calculated as the ratio of cross-plume extent on each side of the centerline $(^{\Delta n}/_{L}) \sum_0^L B_1(n)/B_2(n)$, plume eccentricity calculated as the average length to width ratio $(^{\Delta n}/_{L}) \sum_0^L \Delta n/B(n)$, and plume aspect ratio calculated as the ratio of average plume thickness to the plume width $(^{\Delta n}/_{L}) \sum_0^L H_P(n,0)/B(n)$. The plume width is computed as the centerline-orthogonal distances between plume boundaries $B(n) = B_1(n) + B_2(n)$ with B_1 and B_2 denoting the orthogonal distances from the plume centerline to the outer and the inner edge of the plume boundary (Figure 1c).

2.2.2. Stratification

To explore the response of the plume stratification to the wind forcing, a diagnostic analysis of the buoyancy frequency $N^2 = -g\beta\partial_z S$ within the plume layer is conducted, where β is the salinity expansion coefficient.

$$\partial_t N^2 + \underbrace{u\partial_x N^2 + v\partial_y N^2 + w\partial_z N^2}_{advection} - \underbrace{g\beta(\partial_z u\partial_x S + \partial_z v\partial_v S + \partial_z w\partial_z S)}_{straining} + \underbrace{g\beta\left[\partial_z\partial_x(K_H\partial_x S) + \partial_z\partial_y(K_H\partial_y S) + \partial_z^2(K_V\partial_z S)\right]}_{diffusion} = 0 \quad (1)$$

In (Equation 1) K_H and K_V are the eddy diffusivity coefficients in horizontal and vertical directions. The time rate of change of stratification and its components (advection, straining, diffusion) are computed using the ROMS tracer diagnostics along the plume centerline. Stratification within the plume layer is indexed by the Plume Richardson Number Ri_{pl}.

$$Ri_{pl} = \frac{gH_p}{\rho_0} \frac{\left[\rho(z_p) - \rho(\eta)\right]}{\sum_{j=n,m}\left[V^j(z_p) - V^j(\eta)\right]^2} \quad (2)$$

In (Equation 2), V^n and V^m denote velocities parallel and perpendicular to centerline direction, respectively (Figure 1c, left panel).

The importance of wind forcing depends on how it compares with other terms, and specifically the buoyancy forcing that controls plumes in the absence of wind. Further, the net effect of surface stress on plume stratification depends on the interplay between wind-driven mixing that reduces stratification and wind-induced straining that can increase stratification. The relative importance of wind forcing and the relative contributions of mixing versus straining are quantified by a reciprocal Wedderburn number that compares wind stress with horizontal density gradient. We call this the Plume Wedderburn Number:

$$W_{pl} = \frac{\tau_s}{gH_P^2\partial_y\overline{\rho}} \quad (3)$$

with surface wind stress $\tau_s = \rho_0 u_s^* |u_s^*|$ where u_s^* is the surface friction velocity, ρ_0 is the ambient density, $\overline{\rho}$ is the plume-layer averaged density and $\partial_y\overline{\rho}$ is the wind-parallel density gradient (i.e., alongshore gradient). The Wedderburn Number has been used in a variety of ways in prior plume studies with different formulations (e.g., Jurisa & Chant, 2012; Zhao et al., 2018).

Wind stress is also evaluated by comparing it with interfacial stress at the base of the plume in orientations parallel and orthogonal to the centerline as $(\tau_s/\tau_I)^n$ and $(\tau_s/\tau_I)^m$ where τ_I is the interfacial stress computed at the base of the plume

Table 1
Model Scenarios, With Different Wind Forcing and Outflow Rates ($\tau < 0$ Represents Upwelling-Favorable Winds and $\tau > 0$ Represents Downwelling-Favorable Winds)

Scenario #	Wind forcing	Outflow rate Q ($m^3\ s^{-1}$)	Wind stress τ (Pa)	$R = 100\ \tau/Q$ (kg $m^{-4}\ s^{-1}$)	Channel length Le (m)
1	No wind	10	0	0	150
2	Weak upwelling	10	−0.02	0.2	150
3	Moderate upwelling	10	−0.10	1	150
4	Strong upwelling	10	−0.50	5	150
5	Weak downwelling	10	0.02	0.2	150
6	Moderate downwelling	10	0.10	1	150
7	Strong downwelling	10	0.50	5	150
8	Moderate upwelling	1	−0.10	10	100
9	Moderate downwelling	1	0.10	10	100
10	Moderate upwelling	0.1	−0.10	100	50
11	Moderate downwelling	0.1	0.10	100	50

$$\tau_I^j = \rho_I (A.\partial_z V)_I^j. \quad (4)$$

In (Equation 4) A is the eddy viscosity coefficient and $\rho_I = \rho(z_p)$ is the interfacial density; the superscript $j = n, m$ denotes the gradient direction. The interfacial shear and the eddy viscosity terms are computed using the ROMS momentum diagnostics by integrating the vertical stress divergence term over the interface (between the upper and lower sigma layers closest to $z = z_p$) at each grid point within the active plume patch, then rotated along the n and m directions. The vertical eddy viscosity coefficient A is approximated by dividing $A\partial_z V$ by the shear at the interface (Figure A1, right panel).

2.3. Case Studies

We present several model scenarios with different wind stress and outflow rates (Table 1). Bulk characterization of these wind-influenced plume characteristics is indexed by the ratio between wind stress and river flow $R = 100\ \tau/Q$ obtained from comparing wind scaled by $t.\tau/\rho$ with river scaled by Q/W where $\rho \sim 10^3$ kg/m^3 is water density, $t \sim 10^3$ s is a time scale for wind forcing on surface of plume, and $W \sim 10^2$ m is a scale width for the outflow jet. In model scenarios, we first contrast the no-wind scenario (scenario #1; Basdurak et al., 2020) with upwelling and downwelling winds (scenarios #2–#7) of various strength, that is, weak, moderate and strong winds represented by stresses of 0.02, 0.1 and 0.5 Pa, with common outflow rate $Q = 10\ m^3\ s^{-1}$. Secondly, we contrast plumes formed under different outflow rates ($Q = 0.1$ and $1\ m^3\ s^{-1}$) and common wind strength, that is, 0.1 Pa (scenarios #8–#11). Following Basdurak et al. (2020), the channel length is adjusted for smaller Q to avoid full mixing of the freshwater discharge in the channel.

3. Results

3.1. Horizontal Structure of the Plume

In the absence of winds, an outflow plume is advected upcoast and downcoast by tidal currents, like the wagging tail of a dog (Basdurak et al., 2020). Tidal asymmetry in the centerline plume trajectory is seen in both alongshore and cross-shore directions (Figures 2a and 3): the plume reaches its maximum downcoast/upcoast extent at low/high tide (Figures 3a and 3c), with the plume centerline switching direction during rising/falling tides and leaving behind low-salinity waters as a relict plume (Figures 3b and 3d). Further, the plume extends furthest offshore at low tide (on downcoast side of the mouth) due to the phasing of outflow momentum and stratification. The three-lobe pattern identified in Basdurak et al. (2020) is apparent in the no-wind scenario.

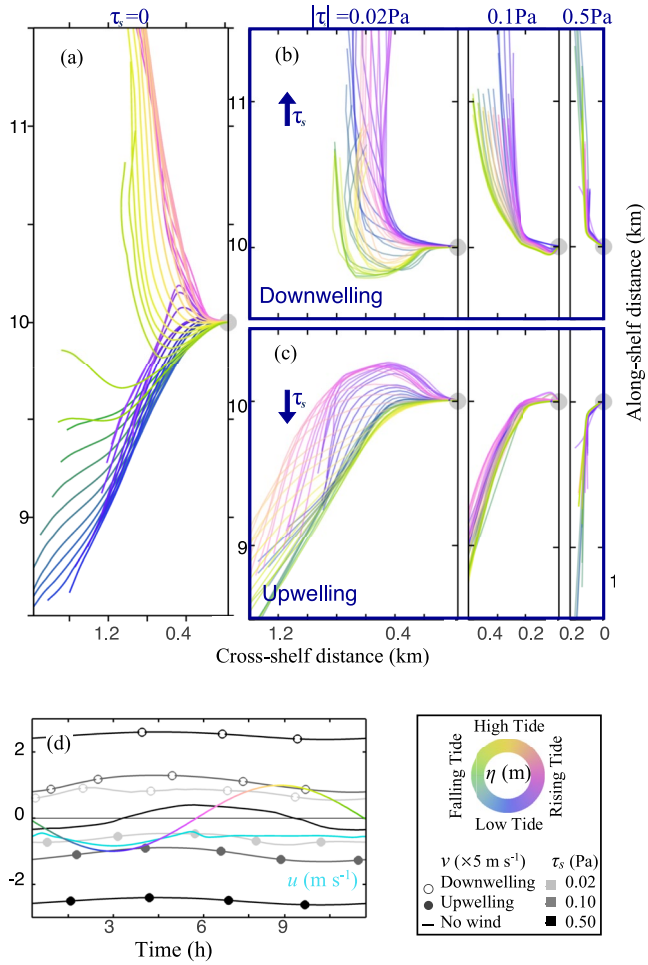

Figure 2. The centerlines for (a) no-wind $\tau_s = 0$, (b) downwelling $\tau_s > 0$, and (c) upwelling $\tau_s < 0$ wind scenarios with tidal phase that is, low, rising, high and falling tides shown in blue, pink, yellow, and green colors, respectively. Each column in (b) & (c) denotes a different wind strength from weak to moderate that is, $|\tau_s| = 0.02$, 0.1, and 0.5 Pa. (d) Tidal surface elevation η (color denotes tidal phase as in panels a–c), surface discharge velocity u at estuary mouth, and scaled ambient along-shelf currents v (values at 4.5 km from shore; marked lines; symbols denoting wind scenario).

With persistent winds the plume no longer switches direction and remains deflected upcoast during downwelling winds and downcoast during upwelling winds. This is true even with weak winds ($\tau = \pm 0.02$ Pa; Figures 2b, 2c, and 3), but significant tidal variability remains. In nearshore waters the plume centerline bends into the wind during the phase when tidally modulated wind-forced alongshore current is weakest (Figure 2d), although these ambient currents do not reverse tidally. As for the no-wind scenario, during upwelling winds plume trajectories extend further offshore (>1 km offshore at high tide) on the downcoast side of the mouth. During downwelling winds plume trajectories extend further alongshore in the upcoast direction.

Wind forcing introduces a marked asymmetry in the plume structure (Figure 3). Strong cross-plume gradients develop along the upwind edge of the plume near the mouth, where one expects an arrested plume front (frontal propagation speed matched by alongshore flow, i.e., Froude Number ~1; Largier, 1992). Surface velocities drop to zero as the alongshore flow approaches this plume boundary, representing subduction of ambient surface flow. Along the downwind edge, the surface salinity gradient is much weaker and broader. Surface velocities are high, exceeding those in the ambient flow. This is an expected response to the surface wind stress, which can strain the shallow plume layer, rapidly blowing low-salinity water downwind.

The apparent bulging of the plume upwind of the mouth is intriguing and associated with the strength of buoyant forcing along this upwind boundary, which can advance the boundary further upwind during phases of weaker alongshore flow. There is a clear upwind curve in the centerline, which is marked owing to how the centerline is defined (not the center of mass for freshwater outflow, but the axis of minimum salinity) and how it aligns with the three-lobe structure of the near-field plume: on rising tides during upwelling winds and on falling tides during downwelling winds, the centerline tracks the center lobe at the mouth and switches to the upwind lobe when it becomes stronger a few hundred meters offshore. However, this tidally varying upwind bulge is clearly apparent in the entire salinity distribution (not only the centerline) and specifically in the movement of the upwind plume edge a few hundred meters upwind of the mouth during tidal phases with slowest alongshore flow (i.e., low tide during upwelling and high tide during downwelling, and persisting into rising/falling phases respectively). This upwind bulging occurs within the coastal boundary layer (i.e., where alongshore ambient flow is reduced–Figure 3b), with maximum upwind extent occurring about 400 m offshore. There is little tidal variability within 200 m of the shore and the upwind plume front contacts the shore about 150 m upwind throughout the tidal cycle.

Similar wind effects are observed in the moderate-wind scenario ($\tau = \pm 0.1$ Pa), with the upwind boundary again sharp and deflected by the alongshore flow while the downwind boundary is diffuse and primarily responding to surface wind stress (Figure 3). Wind forcing appears to dominate and there is very little tidal variability, but still there are some small differences between structure for upwelling and downwelling wind scenarios. The plume is more strongly deflected alongshore due to both wind-driven ambient currents and surface wind stress; the centerline trajectory remains within 500 m of the shore for both upwelling and downwelling scenarios (Figures 2 and 3). Upwind bulging is confined to a narrower coastal boundary layer, that is, within 200 m of the shore, and the upwind plume front (flow convergence) is no more than 100 m upwind of the channel mouth. The three-lobe pattern is feint under moderate winds.

With strong wind forcing ($\tau = \pm 0.5$ Pa) there is negligible tidal variability and plume structure is almost a mirror reflection under upwelling and downwelling wind scenarios (Figures 2b, 2c, and 3). Wind dominates tidal and buoyancy forcing, and the plume is immediately deflected, remaining within 200 m of the shore (centerline

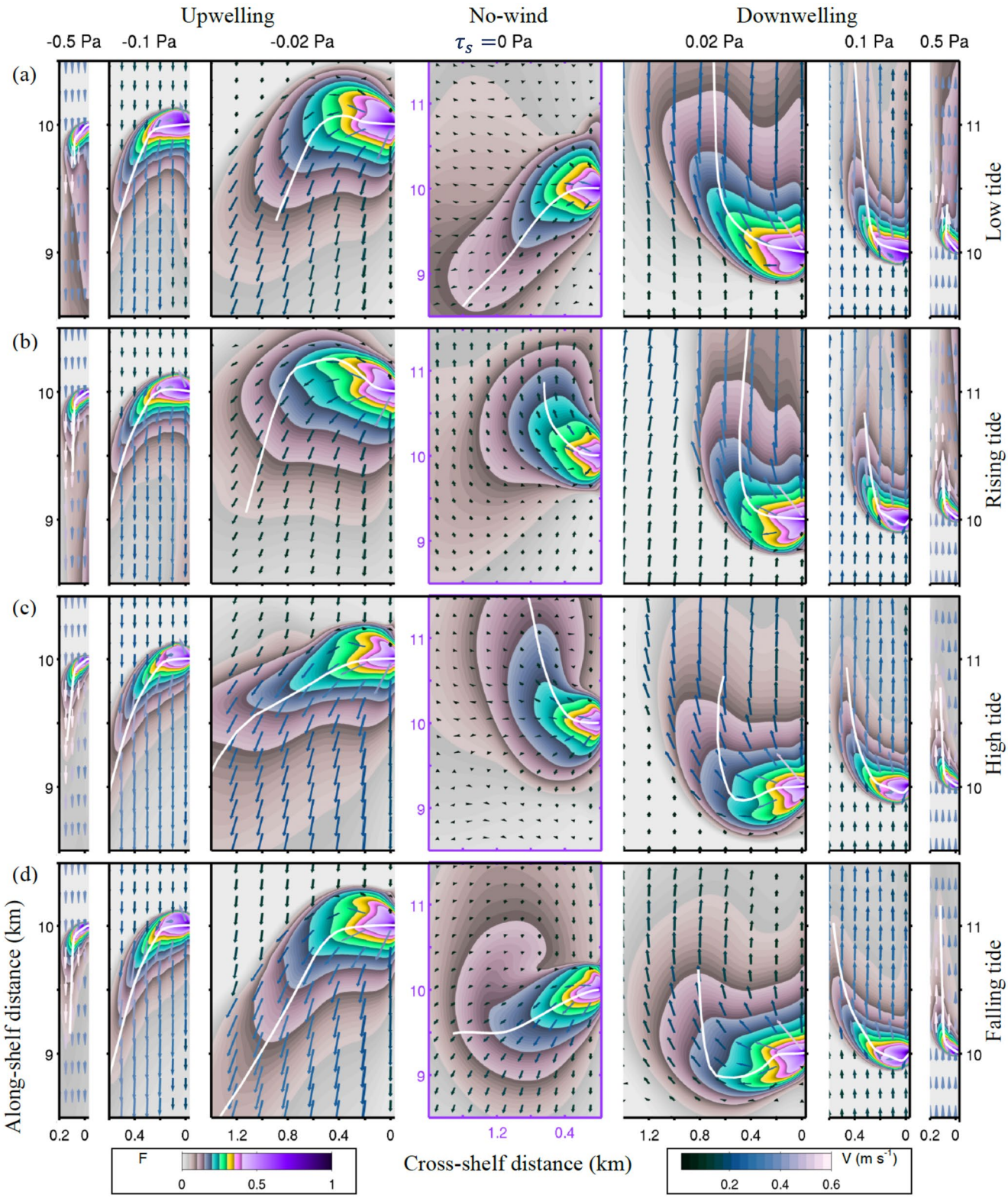

Figure 3. Surface snapshots of surface currents V and outflow fraction F Columns denote upwelling/downwelling wind-intensity (no-wind scenario framed in purple); rows denote four tidal phases, (a) low (b) rising (c) high, and (d) falling tide. Magnitude of flow velocity is shown in color and the size of the arrow. The white thick line is the plume centerline.

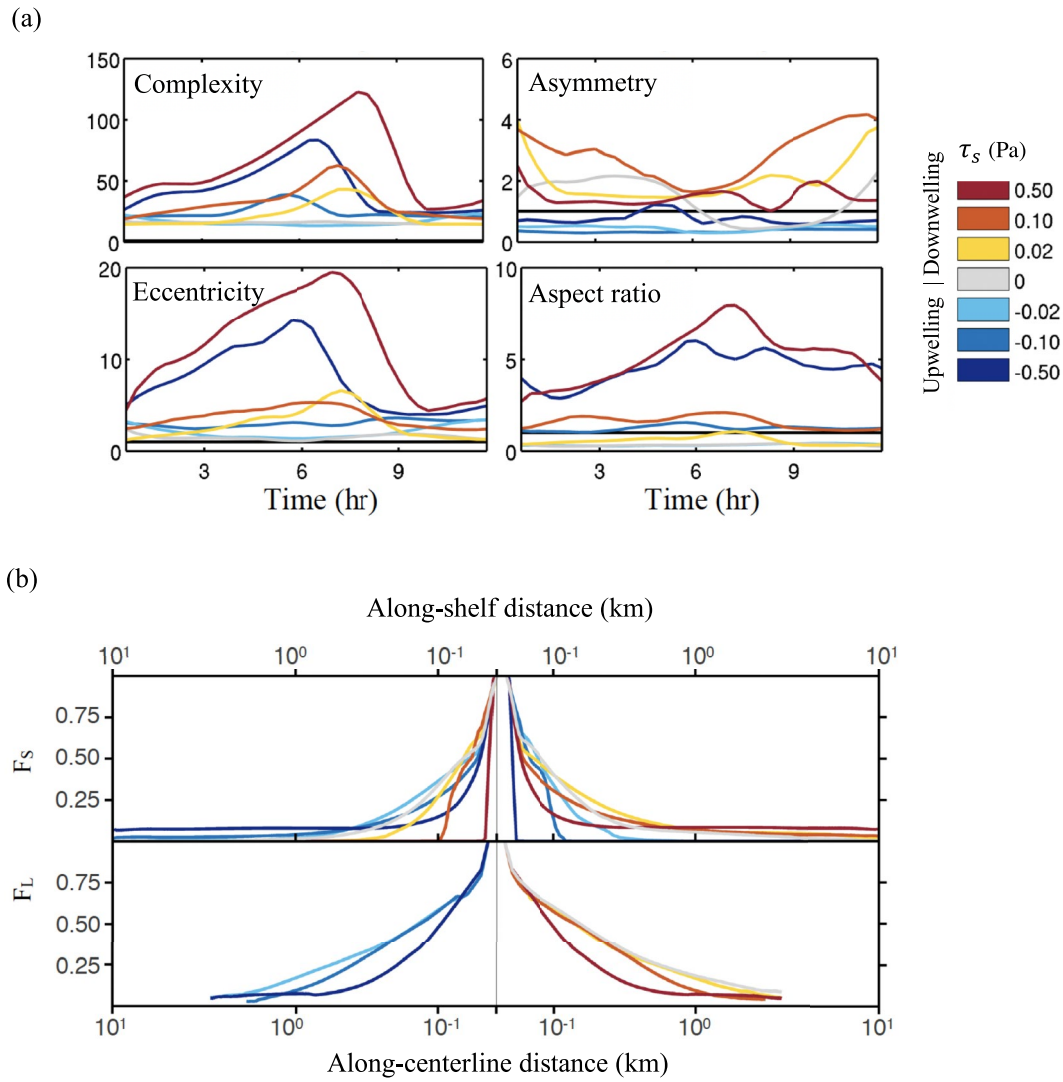

Figure 4. (a) Tidal variation of the plume geometry: complexity (the ratio of squared boundary perimeter to the plume surface area), asymmetry (the ratio of centerline to boundary distances on either side of centerline), eccentricity (average length to width ratio), and aspect ratio (the ratio of averaged plume thickness to the plume width). (b) Tidally averaged outflow fraction F along the shoreline F_S and along the centerline F_L.

parallels shore about 100 m from the shore). There is no upwind bulging (coastal boundary layer <100 m wide), and the upwind boundary is right at the mouth. There is no downwind boundary as the deflection is so strong that the plume boundary remains in contact with the shoreline; however, the extent of shoreline contact varies tidally even under the strongest winds. The three-lobe pattern is absent under strong winds.

The wind-influenced tidal variation in plume structure can be summarized by morphometric indices: complexity (compactness), asymmetry, eccentricity, and aspect ratio (Figure 4a). Under weak and moderate winds, plumes are more compact (less complex) and less eccentric, whereas they become elongated under strong wind forcing (less compact and more eccentric) as well as high aspect ratios (thicker plumes confined to narrower swath). While tidal variability is weak under strong winds (Figures 2b and 2c), there is a notable tidal cycle in the alongshore spreading of the plume (increased eccentricity and complexity, Figure 4a). Maximum elongation occurs during low/rising tides for both upwelling and downwelling strong-wind scenarios (Figure 4a).

The alongshore transport of low-salinity water in river plumes is strongly influenced by wind forcing, with highly diluted waters extending furthest downwind for strongest winds despite the rapid dilution of surface salinities near the mouth (Figure 3). In general plume-water fraction F drops to about 10% within 1 km of the mouth in all

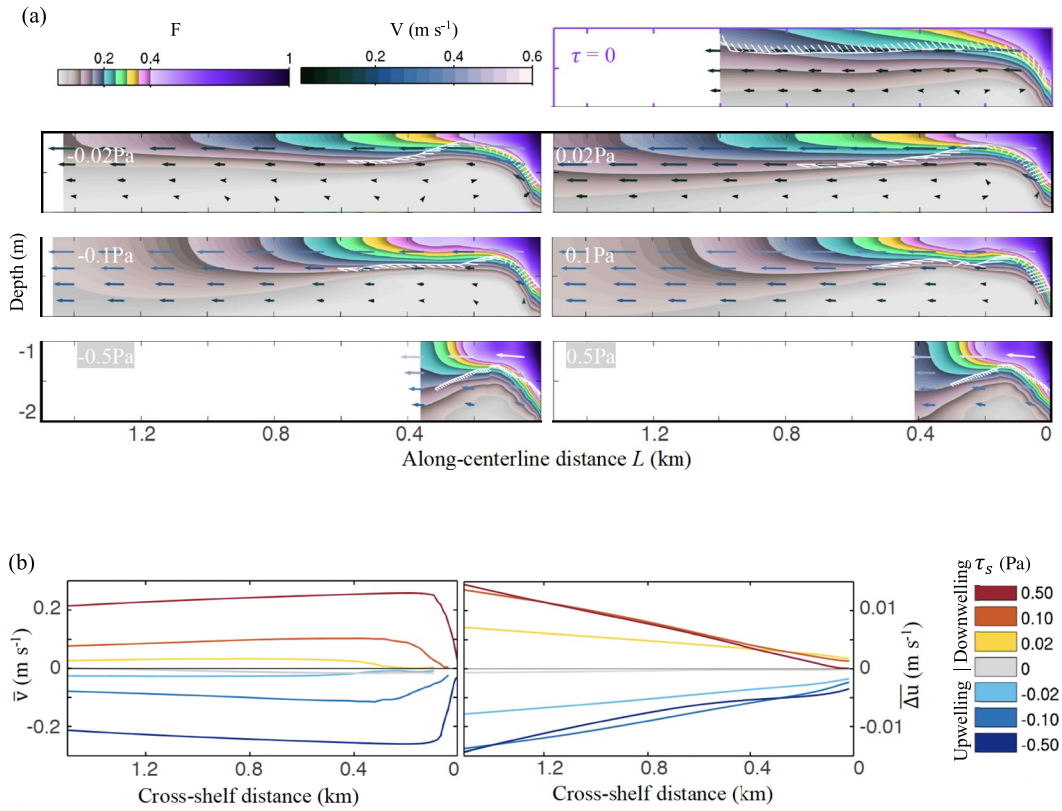

Figure 5. (a) Vertical profiles along the centerlines at low tide; the white-hatched line denotes the plume depth. Upwelling/downwelling winds are shown in the left/right panels with a black frame; the no-wind scenario is shown with a purple frame on the top-right. (b) Tidally averaged cross-shelf top-bottom velocity difference $\Delta\overline{u}$ (right panel) and tidally averaged along-shelf, depth-averaged velocity $\overline{v}$ (left panel) uninfluenced by the plume (values from location 3 km upwind of plume).

scenarios. On the downwind side, closer to the mouth F values are higher for weaker winds (stronger buoyancy forcing and more effective wind-forced straining), but further from the mouth F values are higher for strong winds (rapid alongshore advection of mixed low-salinity water by wind-driven currents)—this is evident in tidal averages of both F_L along the centerline and F_S at the shoreline (Figure 4b). At ~100 m from the mouth F_S is ~0.4 for weak winds and ~0.2 for strong winds, but shore contact with $F_S \sim 0.1$ extends several kilometers downwind only during strong winds. On the upwind side, shoreline plume contact with $F_S > 0.1$ extends about 200 m during weak winds and about 100 m during moderate winds, but negligible during strong winds.

3.2. Vertical Structure of the Plume

There is little tidal variability in the vertical structure of the plume along the centerline, however there are marked differences between wind scenarios (Figure 5a). In the absence of wind forcing the plume thins gradually and monotonically after lift-off (Figure 5a, top right panel). With wind forcing, the plume thins immediately after lift-off (as for no-wind scenario) but then thickens further downstream due to wind induced mixing. With stronger winds, the plume thickens more quickly and isopycnal slopes are steeper at the downstream end of the plume. Stronger winds also result in dilution occurring closer to the estuary mouth: $F = 0.2$ isoline occurs ~400 m from mouth for strong winds but ~700 m from mouth for moderate winds and >800–1,000 m for weak winds and no-wind. However, it is notable that the high-F inner plume extends further downstream under weak/moderate winds than either no-wind or strong-wind scenarios: at the surface the $F = 0.3$ isoline extends ~400 m in the absence of wind and only ~300 m during strong winds, but exceeds 500 m for both weak and moderate winds.

In contrast to observations of larger plumes, there is little difference between plume width and offshore position for upwelling versus downwelling wind scenarios (Lentz & Largier, 2006). This is evidenced by the centerline positions in cases of moderate to strong wind stress (Figures 2b and 2c). Wind-driven Ekman effects are weak

or absent in the plume given short time scales and strong surface currents parallel the shore (Figure 3). Further, Ekman effects in the ambient flow are weak nearshore, which is pertinent because the plume is deflected quickly and remains close to the shore. Offshore in deeper waters a well-developed Ekman layer is evident and strong quasi-geostrophic alongshore flows occur, but nearshore the water is shallow and the shore is nearby resulting in slower alongshore currents (i.e., coastal boundary layer, Nickols et al., 2012) and weak/absent Ekman transport and vertical circulation (Figure 5b; Kirincich et al., 2009). For weak winds, the plume extends far enough offshore to be subject to some influence from Ekman transport, explaining the marked difference between upwelling and downwelling winds (Figures 2b, 2c, and 3). However, for stronger winds, the plume remains within a few hundred meters of the shore and is not significantly exposed to wind-driven vertical circulation in the ambient flow (top-bottom velocity difference is order 1 mm/s), thus explaining the similarity between upwelling and downwelling scenarios. Further, in contrast to the paradigm for large-scale plumes, far-field plumes are not shore attached nor bottom attached and winds do not accelerate the plume through steepening isopycnals and surface slope as outlined by Moffat and Lentz (2012).

Stratification at the base of the plume responds to wind forcing due to the relative contribution of advection, straining and diffusion (Equation 3). Tidal-average values of these terms are calculated along the plume centerlines and plotted as a function of F (Figure 6a). Advection and straining increase stratification whereas diffusion reduces it, with all terms weakening with distance away from the mouth (as F decreases). Straining becomes weakly negative in the far-field for strong winds ($F \sim 0.2$), related to cross-shore steepening of isopycnals and convergences. All effects are stronger with stronger winds, specifically straining and diffusion near the mouth ($F > 0.7$) where terms are an order of magnitude stronger than for weaker winds or further from the mouth. The correlation between absolute values of advection, diffusion and straining are shown for different wind direction and strength (Figure 6b). Advection increases with wind speed, directly proportional to diffusion and straining, except for the relatively high advection values near the mouth for moderate downwelling winds—and stronger diffusion versus straining (Figure 6b).

Vertical profiles along the centerlines also reflect the influence of straining. Downstream extent of the high-F inner plume exceeds 500 m for both weak and moderate winds due to the wind-driven straining after the plume is deflected from shore-normal orientation (along-plume straining is not expected close to the mouth as wind stress is orthogonal to plume axis). Under moderate winds the positive effect of straining is only evident where $F > 0.3$ (i.e., buoyancy strong enough), whereas the positive effect of straining is evident even in the outer plume under weak winds ($F \sim 0.1$ extends ~1.5 km downstream)—this is also evident in Figure 4b. Wind stress plays a key role in mixing large plumes by modifying their geometry; more importantly, depending on its direction local winds can produce larger net mixing then wave-driven dynamics (Kastner et al., 2018).

3.3. The Relative Importance of Wind Forcing

Wind forcing affects small plumes in several ways, including direct forcing (surface stress), vertical mixing, straining, and deflection by wind-driven ambient currents—each effect depending on the strength of wind relative to buoyancy forcing and other terms and varying spatially across the plume (Figure A2).

The upwind edge of the plume is deflected by wind-driven alongshore flow, forming an arrested plume front bulging upwind of the mouth when wind forcing is weak. Along this front, buoyancy is balanced by alongshore advection (internal Froude Number ~1), with dense ambient water subducting beneath the buoyant plume and surface velocity ~0 along the front (Figures 3 and A1). A front also forms along the upwind edge of the plume for moderate and strong winds but does not extend much upwind of the mouth, and it is marked only within ~100 m of the shore. Inshore of the upwind maximum, the plume is similar to the no-wind scenario. Offshore of the upwind maximum, the front curves downwind and weakens/broadens as plume water mixes and the density deficit (i.e., density difference between plume and ambient waters) decreases, as observed in a classic buoyant jet in a crossflow (e.g., Jirka et al., 1981) with little apparent influence of the local wind stress. Downwind of the frontal edge of the plume, direct wind forcing (i.e., surface stress) becomes more important (Figure 7), evident in enhanced surface velocities in the plume where momentum is retained in a thin surface layer (Figure A1), and in the orientation of surface velocity parallel to the shore/wind orientation for moderate and strong winds.

The importance of surface stress is also evident in the spatial pattern of W_{pl} (Figure 7), showing that wind stress dominates buoyancy forcing in the far-field. W_{pl} values are low along the upwind frontal boundary, where

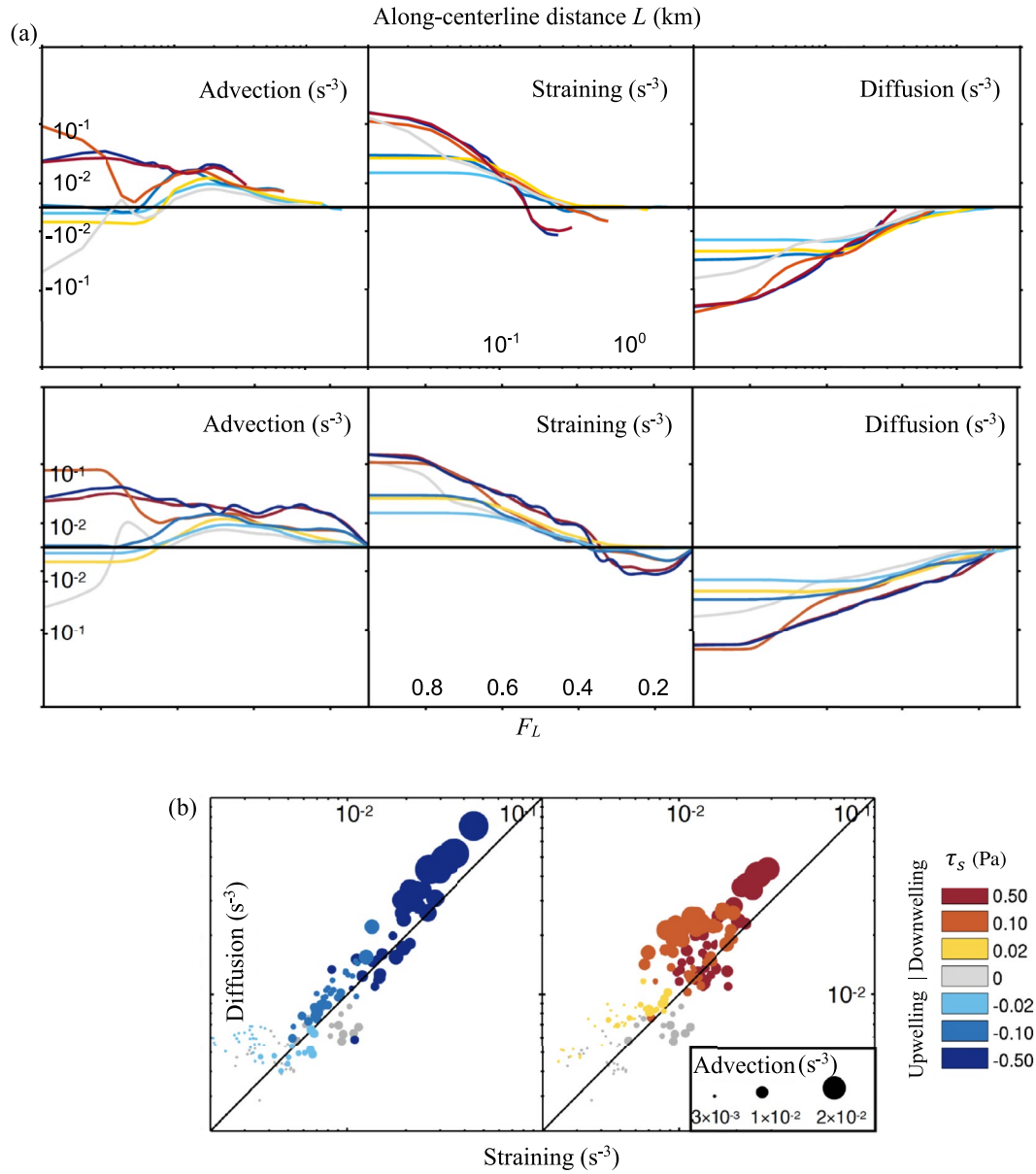

Figure 6. Tidally averaged components of the plume stratification $\partial_t N^2$ in s^{-3}. (a) Advection, straining and diffusion along the centerline as a function of distance L (top panel) and as a function of the outflow fraction F_L (bottom panel). Positive/negative values denote the tendency to increase/decrease stratification. (b) Diffusion versus straining with marker size denoting the magnitude of advection. All the axes in (a), (b) except F_L are shown in log-scale.

buoyancy dominates, as well as near the mouth. However, away from the mouth and upwind boundary, $W_{pl} > 1$ and surface wind stress is locally dominant relative to buoyancy forcing. This is true for all wind strengths, although more marked for stronger winds and wind dominance generally increases with distance from the mouth (as buoyancy effects weaken owing to mixing). The exception is during low and rising tides with weak downwelling winds, when the plume is very thick (Figure A2), $W_{pl} < 1$ and buoyancy is again important in the far-field. Consistent with W_{pl} spatial patterns, interfacial stress is comparable or bigger than the surface stress near the mouth and along the upwind frontal boundary where shear is strong at the base of the plume layer ($\tau_I > \tau_s$, Figure 8). The remainder of the plume area is dominated by surface wind stress ($\tau_I < \tau_s$), specifically in the along-plume orientation.

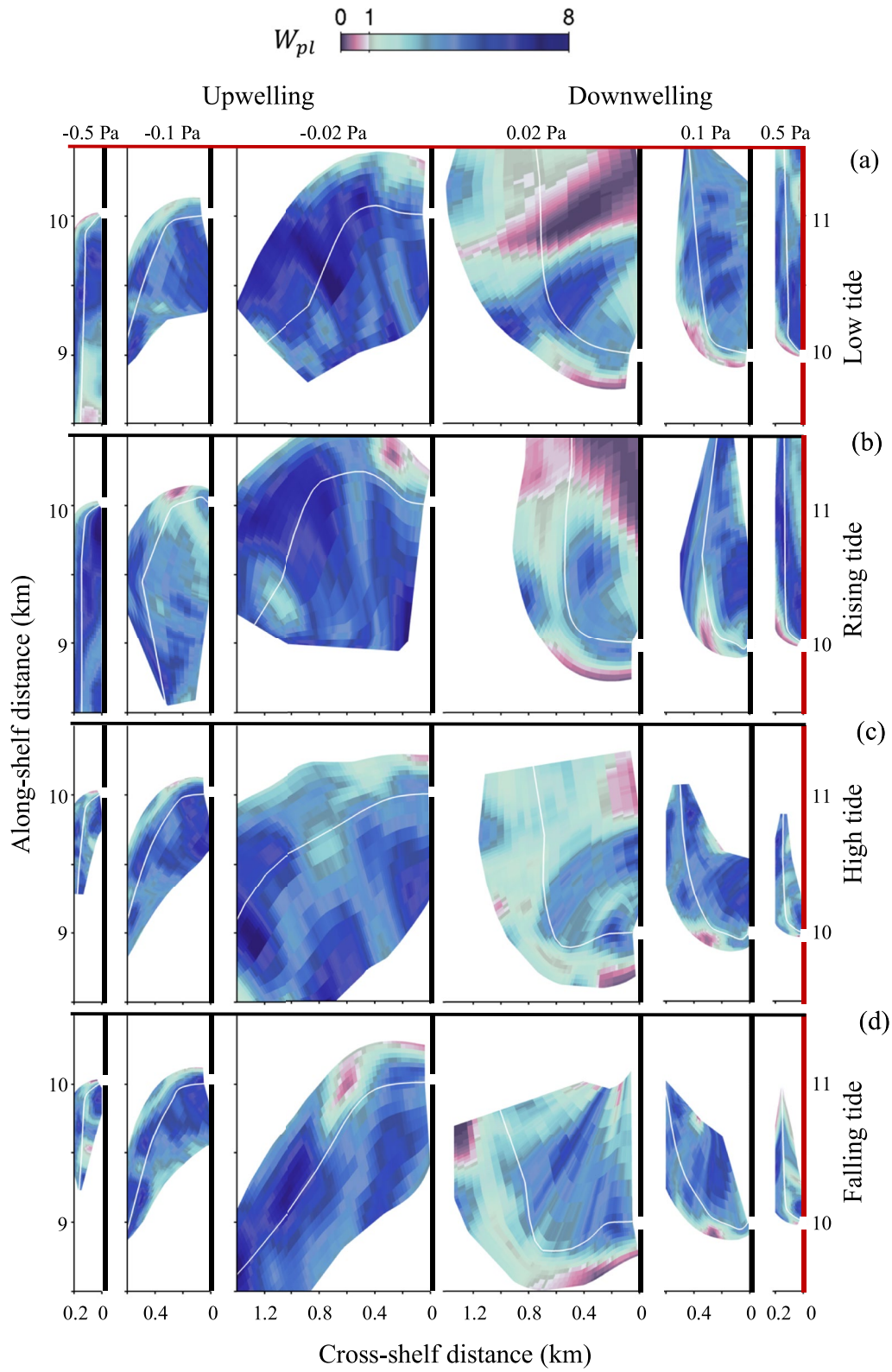

Figure 7. Snap-shots of the Plume Wedderburn Number W_{pl} for different wind scenarios and tidal phases.

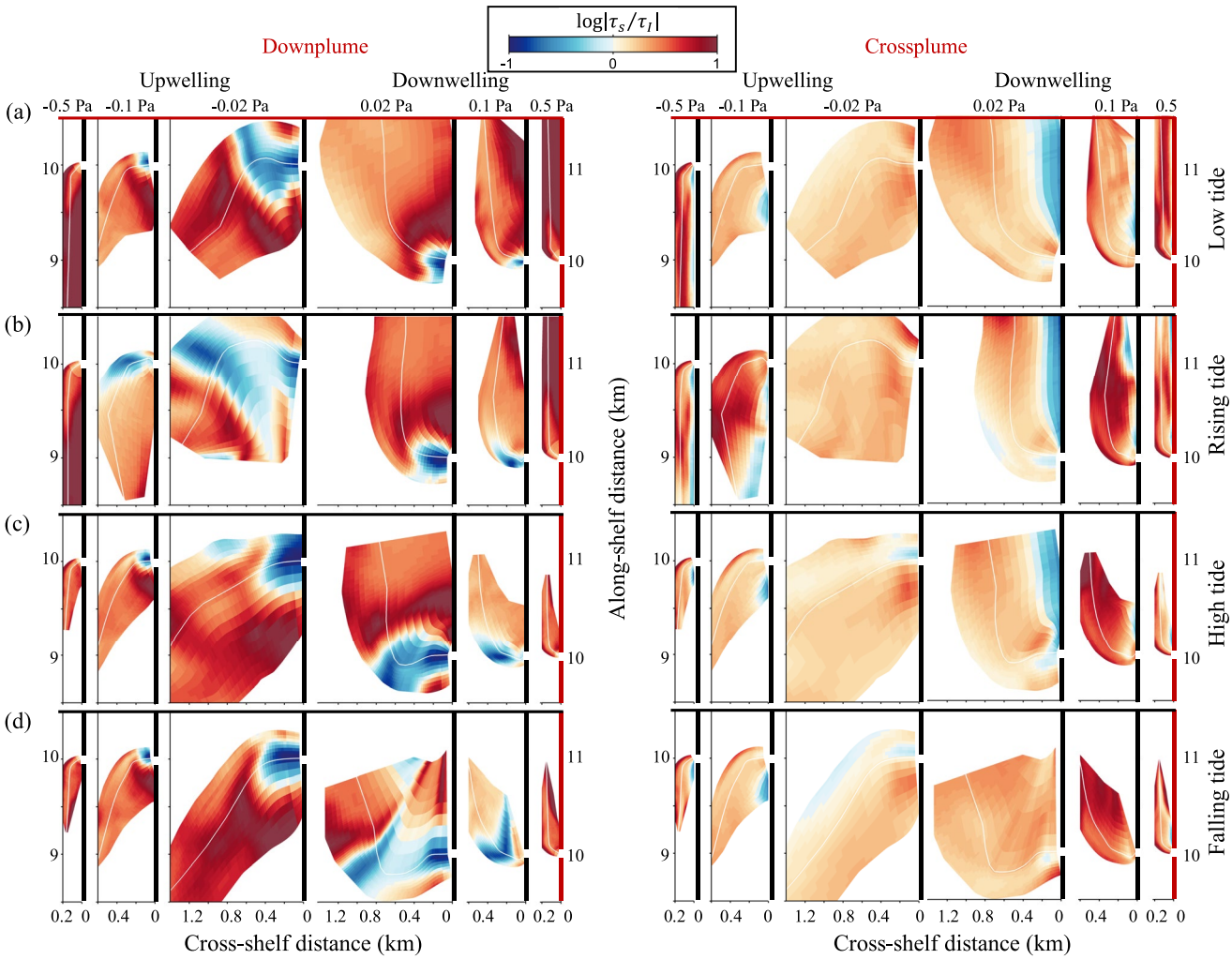

Figure 8. Snap-shots of the ratio between wind stress and interfacial stress for different wind scenarios and tidal phases; down-plume and cross-plume components are shown in left and right panels, respectively.

The vertical stability of the plume depends on density stratification versus surface and interfacial stresses. Within the plume, stability is assessed with the plume Richardson Number Ri_{pl} which compares stratification in the plume layer versus shear in that layer: the stronger the stratification the stronger the shear that can be supported and thus the greater the straining of the plume layer (Figure 9). Near the mouth, buoyancy effects can withstand surface stress ($W_{pl} < \sim 1$, Figure 7) and the plume layer is stable ($Ri_{pl} > 1$, Figure 9), extending ~1 km offshore and downwind during weak winds, but reduced to <½ km during moderate wind forcing and imperceptible during strong winds.

Tidal variations are evident during weak winds, partly related to the interaction between the three-lobe pattern and the ambient flows in the upwind and downwind directions (Figures 3 and 9). During low and rising tides with weak/moderate downwelling winds, the plume layer is more mixed along the centerline than either side of the centerline—likewise during high and falling tides with upwelling winds (Figure A1, left panel).

In the areas where $Ri_{pl} > 1$, it can expected that the plume layer is strained by surface wind stress, which is consistent with the longer reach of low-salinity surface water under wind forcing relative to the no-wind scenario (Figure 3): this effect is absent for strong winds, strongest for moderate winds up to a distance of ~½ km, and strongest for weak winds beyond that to distances exceeding 1 km. While the effect of straining is seen in the salinity field a little beyond the point where $Ri_{pl} = 1$, in the outer plume where $Ri_{pl} < 1$ the plume layer is well mixed, and it moves as a coherent layer. Here the plume is forced by the combination of surface wind

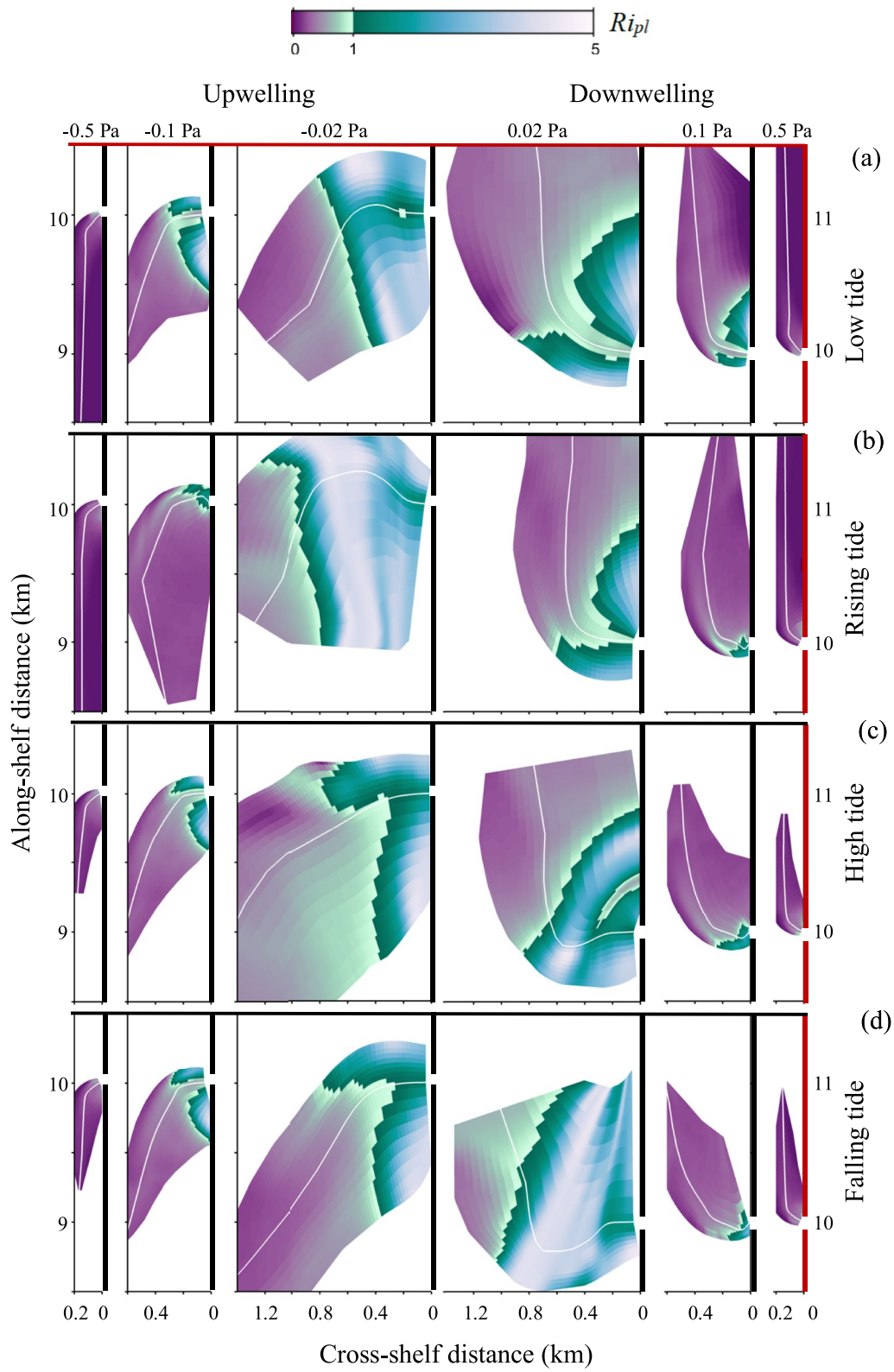

Figure 9. Snap-shots of the Plume Richardson Number Ri_{pl} for different wind scenarios and tidal phases.

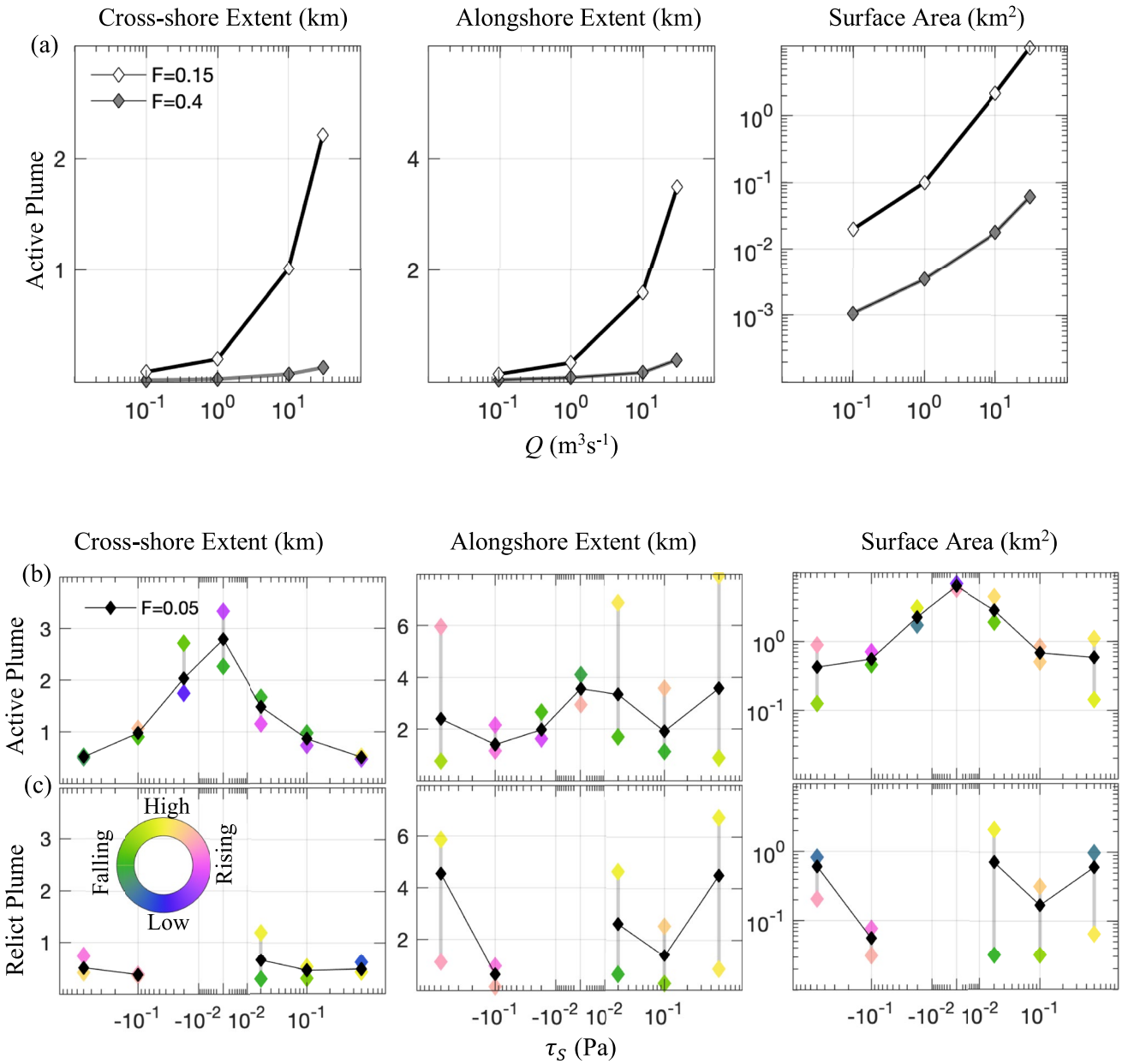

Figure 10. Extent of plume in alongshore and cross-shore directions (left and middle panels), and its surface area (right panel) (a) without wind forcing $\tau_S = 0$ and (b), (c) with constant $Q = 10$ m^3 s^{-1}. Tidal variability (b), (c) is shown with a vertical bar and the tidal phase of the extremum is marked by colored markers for (b) active plume (horizontal black lines denote the tidal averages) and (c) relict plume. The analysis is based on F–dependent plume boundary: (a) $F = 0.15$ and $F = 0.40$, and (b), (c) $F = 0.05$.

stress, interfacial stress and buoyancy forcing—and as described above, surface stress exceeds interfacial stress (Figure 8) and surface stress dominates buoyancy forcing (Figure 7) so that the plume waters are predominantly wind forced and residual/diluted freshwater is advected as a passive constituent.

3.4. Spatial Extent of Plume

Runoff from small rivers creates small plumes, covering an area of a several square kilometers over a tidal cycle (Figure 10a). With alongshore wind forcing, these plumes are deflected to one side, with weak or no tidal variability so that they impact a smaller surface area. Offshore extent is reduced by deflection (Figure 3) and the tide-aggregated alongshore exposure is also reduced as the plume remains on one side of the mouth. When the

plume extent is defined by the $F = 0.05$ tide-averaged boundary, an outflow of 10 $m^3\ s^{-1}$ produces a plume with surface area ~6 km^2, which is reduced to ~1 km^2 with moderate or strong winds (Figures 10b and 10c). This boundary extends furthest offshore in the absence of wind (>2 km) and less so when winds deflect the plume, being reduced to <1 km for strong winds. And while the $F = 0.05$ tide-aggregated boundary extends ~3.5 km alongshore in the absence of wind, with deflection by wind forcing the alongshore extent is reduced to <2 km (plume remains on one side of the mouth).

However, the tendency for greater upcoast extent due to tidal phasing in water depth and outflow (Basdurak et al., 2020) is enhanced by weak downwelling winds so that alongshore extent is ~3 km whereas this tendency is countered by weak upwelling winds and alongshore extent is ~2 km. Similarly, the tidal effect that produces greater offshore extent when plume is downcoast (Figure 3) persists during weak upwelling winds so that the tide-average offshore extent is ~2 km for weak upwelling winds, but <1.5 km during weak downwelling winds. Alongshore extent is shortest for moderate winds (<2 km), which negate these tidal effects and during which plume waters mix and are diluted faster. However, for strong winds the mixed plume waters are strongly/passively advected alongshore and the $F = 0.05$ boundary can extend 2–3 km alongshore. This is also seen in how F values decrease along the centerline and shoreline (Figure 4b), with high F values extending the furthest alongshore under weak winds, but low F values extending furthest alongshore under strong winds—the transition occurs at ~½ km along the shoreline and ~2 km along the centerline.

Tidal variability of the plume extent (defined by $F = 0.05$ boundary; colored markers in Figures 10b and 10c) reveals maximum (minimum) offshore reach at falling (rising) phase during downwelling winds (vice versa during upwelling winds). Moderate and strong downwelling winds extend the plume upcoast furthest at high/rising phase. In addition to the active plume (plume waters attached to the river mouth), distinct relict plume patches are observed at the shoreline for strong winds (Figure 10c). These relict plumes are more notable for downwelling scenarios, extending about 7 km downwind with strong winds at high tide. During weak upwelling winds they do not develop.

For rivers with weaker outflow, a plume forms with a similar shape (Figure 11)—and even with moderate winds these plumes show little tidal variability. For $Q = 1\ m^3\ s^{-1}$ the upwind frontal edge is evident as well as mixing and straining downwind of the centerline, whereas for $Q = 0.1\ m^3\ s^{-1}$ the detail of the 10 m-scale plume is not evident in this 5 m-resolution model. Given the model bathymetry the cross-shore extent of the plume for $Q \leq 1\ m^3\ s^{-1}$ is expected to be smaller than the expected width of a surf zone and the plume may be trapped in the surf zone where wave forcing is strong (e.g., breaker height of 1–2 m). However, here we compare the plume for $Q \leq 0.1\ m^3\ s^{-1}$ and $Q \leq 1\ m^3\ s^{-1}$ in the absence of wave forcing and show that the zone of impact for pollutants is markedly different: the former is shore attached while the latter is shore detached. With a 10-fold reduction in outflow, the $F = 0.15$ plume area shrinks from ~2 km^2 for $Q = 10\ m^3\ s^{-1}$ to ~0.1 km^2 for $Q = 1\ m^3\ s^{-1}$ and further to ~0.02 km^2 for $Q = 0.1\ m^3\ s^{-1}$. At the same time the alongshore extent decreases from 1.5 to 0.2 and 0.1 km, respectively and cross-shore extent is reduced from 1 to 0.5 and 0.25 km, respectively (Figure 10a).

4. Discussion

Small rivers and creeks with modest discharge yield small plumes that are readily deformed by ambient tidal currents, but they are also highly susceptible to wind forcing, responding more quickly than larger and thicker river plumes. We have explored the effect of alongshore winds, which are often dominant along the mountainous coasts characterized by numerous small rivers and creeks. We show that even under weak wind forcing the plume is deflected to one side of the river mouth throughout the tidal cycle (Figure 3). The plume is deflected by both wind-driven alongshore currents and by the direct effect of surface wind stress. The upwind boundary is primarily deflected by the ambient current, being deflected downwind and strengthening into a sharp arrested plume front (Froude Number ~1). As the plume stretches offshore and weakens, so does this upwind boundary; it curves downwind and the frontal gradient weakens. The ambient flow subducts at this upwind edge and asserts an interfacial stress beneath the plume. However, downwind of this boundary, interfacial stress weakens, and surface wind stress is dominant (Figure 8). It accelerates the alongshore movement of plume waters, which move faster than ambient waters as wind-supplied momentum is contained in the thin plume layer. Further, the wind can strain the plume layer itself close to the mouth where density differences are large enough to prevent

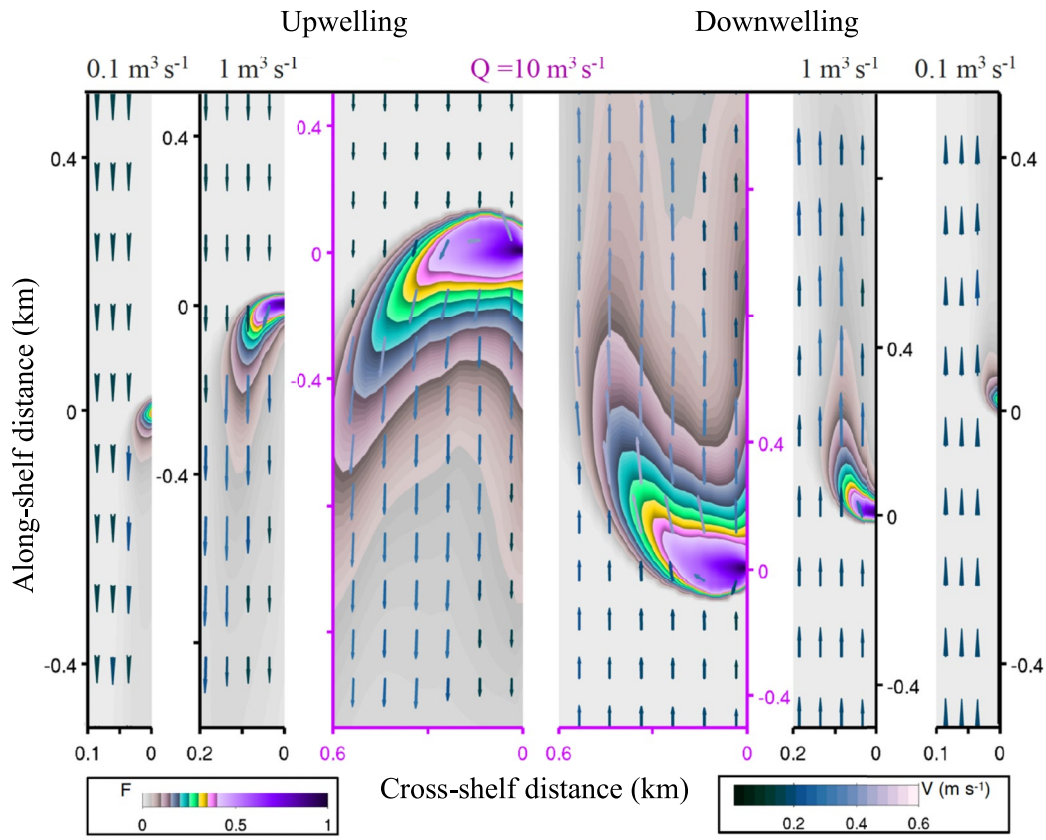

Figure 11. As in Figure 3, showing plumes at low tide with wind stress $\tau_s = 0.1$ Pa, but different outflow rates $Q = 0.1$, 1, 10 m^3 s^{-1} at low tide.

wind-driven vertical mixing. This straining and elongation of the surface salinity field occurs over the longest distance for weaker winds (apparent as far as $F \sim 0.2$), but the straining is stronger in the inner plume with moderate winds. This straining is expected where the Plume Wedderburn Number is low (Figure 7) and it is observed along centerline transects where high F values extend the furthest where straining is most effective (Figure 5a). In the outer plume, where the Plume Wedderburn Number is large and surface wind stress dominates residual buoyancy effects, the plume is mixed ($Ri_{pl} < 1$, Figure 9) but still exhibits a pycnocline akin to a surface mixed layer. Here the diluted outflow waters continue to move downwind, advected by wind-driven currents as a passive constituent.

The innermost plume is least influenced by wind forcing, initially dominated by the inertia of the outflow and quickly responding to strong buoyancy effects in the same way outlined for the tidal plume by Basdurak et al. (2020). Here wind stress is cross-plume, interacting with very strong density gradients so that the Plume Wedderburn Number is small (i.e., buoyancy dominates over wind forcing). However, the momentum of the wind-driven alongshore flow is significant, and the upwind boundary is quickly deflected, specifically for moderate/strong winds (curving downwind within 100 m of the mouth for strong winds). The plume zones defined by Basdurak et al. (2020) for a tidal plume are altered by wind forcing. In the presence of wind forcing, we differentiate between the near-field plume that is characterized by outflow inertia and buoyancy forcing (like a classical buoyant jet) and the mid-field plume that is characterized by surface wind stress and stratification with low Plume Wedderburn Number such that straining is important. In the far-field plume, wind stress overcomes stratification (high Plume Wedderburn Number), resulting in vertical mixing and passive alongshore transport of diluted outflow waters by a wind-driven alongshore current.

The shape and size of the plume is important in controlling exposure of nearshore habitats to runoff effects, including the potential exposure of humans to pathogen pollution. With wind forcing the plume is deflected, offshore extent is reduced, and the plume only impacts one side of the mouth, most notable in the pattern of

shoreline contact (Figures 4b and 10). Wind strength has two effects, increasing near-field dilution so that outflow concentration decreases quickest for strong winds, but also advecting mixed outflow waters alongshore so that outflow concentration is greatest in the far-field under strong winds. An intriguing additional effect of wind is the occurrence of relict plumes—nearshore patches of diluted outflow water detached from the active plume and advected far alongshore (~8 km in strong-wind model scenarios). This phenomenon appears to arise from small tidal differences in outflow velocity due to changes in depth of the outflow channel. The shore-attached relict plume develops during low tide when the downwind-lobe is well developed and injects water along boundary with little offshore momentum (Figure 3), but subject to alongshore wind stress. While this part of the plume exhibits low initial concentrations, it is blown downwind with little further lateral or vertical mixing and F values exceeding 0.05 are observed several km downwind (Figure 10), representing shoreline exposure to plumes far from their origins—although this effect is likely disrupted in the presence of wave forcing and rip currents (e.g., Clarke et al., 2007). Relict plumes may also be disrupted by eddy stirring that can affect surf-zone circulation as outlined by Kumar and Feddersen (2017).

Small plumes are thinner than large ones and not much influenced by Coriolis, which makes them more susceptible to wind effects (Figure A2). Larger outflows extend far offshore with strong inertia compared to wind intensity, causing big differences between upwelling (shore-detached, broadening) and downwelling (shore-attached, narrowing) favorable conditions due to wind-driven Ekman transport for example, Columbia River plume (Garciá Berdeal et al., 2002; Hickey et al., 2005). Wind intensity affects plume width, thickness, and propagation speed (Lentz & Largier, 2006; Rijnsburger et al., 2018). However, in the case of strong winds and weak outflow, the plume is deflected quickly and advected alongshore without exposure to the effects of Ekman transport. Under these circumstances, upwelling and downwelling conditions exhibit similar patterns, that is, a passive plume advected alongshore by strong currents. We compare our small-plume model results with model results from Fong and Geyer (2002) and observations from Lentz and Largier (2006), specifically showing differences in plume geometry, stratification, and propagation speed, and importance of wind (Figure 12). In the absence of wind, plumes are broad and thin (large aspect ratios, Figure 12a). Small plumes exhibit marked tidal variations but typically aspect ratios are more than double those for large plumes (i.e., wider spread for given plume thickness), specifically for weak/upwelling winds. With strong/downwelling winds, small plumes are confined close to shore and mixed deeper, yielding smaller aspect ratios more comparable with large plumes. Small thin plumes are quickly strained by winds, resulting in more shear and mostly smaller Plume Richardson Numbers (Figure 12b). In the absence of wind, $\mathrm{Ri}_{\mathrm{pl}}$ approaches one for small plumes, whereas Ri_{pl} often exceeds one for large plumes when the winds are weak. While larger plumes propagate at speeds close to the buoyancy-controlled internal-wave speed, tidal and wind forcing of small plumes account for propagation speeds that exceed the internal-wave speed. Small plumes propagate downwind at speeds two to three times that of the internal wave speed, with faster propagation during string winds (Figure 12c). The importance of surface wind stress relative to buoyancy effects is indexed by the Plume Wedderburn Number (Figure 12d), showing that wind stress is twice as important in modeled small plumes (this work) than in modeled larger plumes (Fong & Geyer, 2002).

The three-lobe pattern identified by Basdurak et al. (2020) is again evident near the mouth, even in the presence of wind forcing. This feature is also observed in satellite imagery presented by Salcedo-Castro et al. (2020, Figure 1). This phenomenon appears to account for relict patches of plume water injected into the nearshore and blown alongshore with little mixing, resulting in plume waters being observed several kilometers downwind with dilution of less than 20-fold. The interaction of the 3-lobe pattern with wind forcing is interesting as the downwind lobe feeds into the nearshore as described above, while the middle lobe is strained and mixed so that it weakens quicker than the upwind lobe that appears to be maintained by convergence along the upwind boundary. This is seen in a few scenarios where the plume centerline (defined as axis of salinity minimum) shifts upwind abruptly where the upwind lobe becomes more intense than the middle lobe (Figure 2; weak wind scenarios).

In summary, small plumes respond strongly to wind forcing. Three zones can be identified: a near-field zone dominated by inertia and buoyancy altered little by wind forcing; a mid-field zone in which the plume is deflected by wind-driven ambient flow and strained by surface wind stress in combination with buoyancy; and a far-field zone where buoyancy is weak, the plume is mixed by wind, and plume waters are passively advected by wind forcing and wind-driven ambient currents. The upwind boundary is deflected and sharpened by wind-driven alongshore flow, which subducts and forms an intense plume front. The downwind boundary is diffuse due to

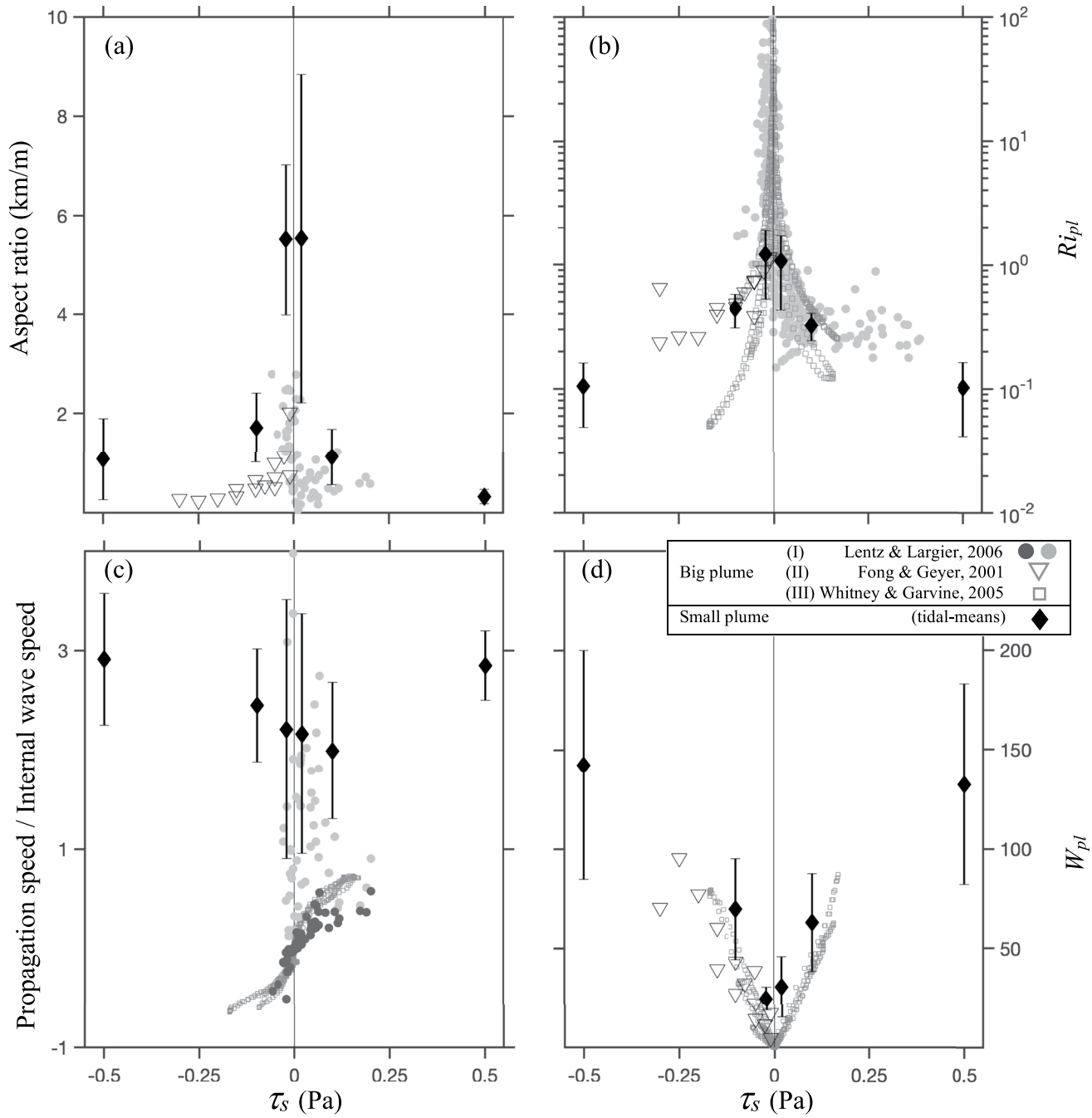

Figure 12. Comparison of the characteristics of small plumes (vertical bar denotes the tidal extent; with spatial averages based on the outflow fraction $F = 0.05$) and big plumes for upwelling ($\tau_s < 0$) and downwelling ($\tau_s > 0$) winds. (a) the aspect ratio given by plume width to plume thickness, (b) the Plume Richardson Number Ri_{pl}, (c) the ratio of plume propagation speed to internal-wave speed with darker filled circles referring to wind driven only speeds, (d) the Plume Wedderburn number W_{pl}. In (b)–(d) the big plume data (II, III) are approximated for steady-state conditions. The Ri_{pl} for (III) as $\phi/\rho U_{wind}^2$ and the scaled propagation speed as U_{wind}/KU_{dis} with the potential energy anomaly ϕ, the buoyancy- and wind-driven velocity scale (U_{dis} and U_{wind}) and the dimensionless current width K (=2 i.e., dataset-specific value). The W_{pl} for (II) is approximated as $(|\tau_s|/\rho)t_s B/Q$, with plume width $B = \left(2Qg_0' f^{-3}\right)^{1/4}$, Coriolis parameter f, reduced gravity g_0' at the mouth, and characteristic time scale t_s; and for (III) as $(|\tau_s|/\rho)U_{dis}K^6/2Qf^2$.

wind stress first straining and then mixing plume waters; in weaker winds the plume is stretched downwind by straining whereas in stronger winds vertical mixing is more important. Due to rapid deflection, small plumes do not extend far offshore and are not subject to Coriolis effects so that upwelling and downwelling scenarios look very similar (mirror reflection) and plumes extend far alongshore. Specifically, there is extensive shore contact

under stronger winds, extended further by relict plume patches advected downwind close to the shore. Following Warrick and Farnsworth (2017) finding that the probability of coalescence is higher in moderate-sized plumes than big plumes, we speculate that small plumes may merge, resulting in a continuous runoff impact in the coastal boundary layer along mountainous coasts where river mouths are closely spaced—a topic for future research.

Appendix A: Plume Layer Characteristics

A1. Thickness and Interfacial Mixing Coefficient

Tidal snapshots of plume thickness accompanying Figure 3 are shown in Figure A1 (left panel). After thinning associated with lift-off, the plume thickens in down-plume direction due to wind-driven mixing. Limited thickening occurs for weak winds (H_p < 1 m in far-field) and it is more pronounced for stronger winds (H_p < 2 m in far field). Greater vertical mixing is evident in higher interfacial mixing coefficients (Figure A1, right panel). Interfacial mixing coefficient is greater for stronger winds and most pronounced at the upwind edge of the plume where shear is high. Interfacial mixing can also be high further downwind, specifically during downwelling winds.

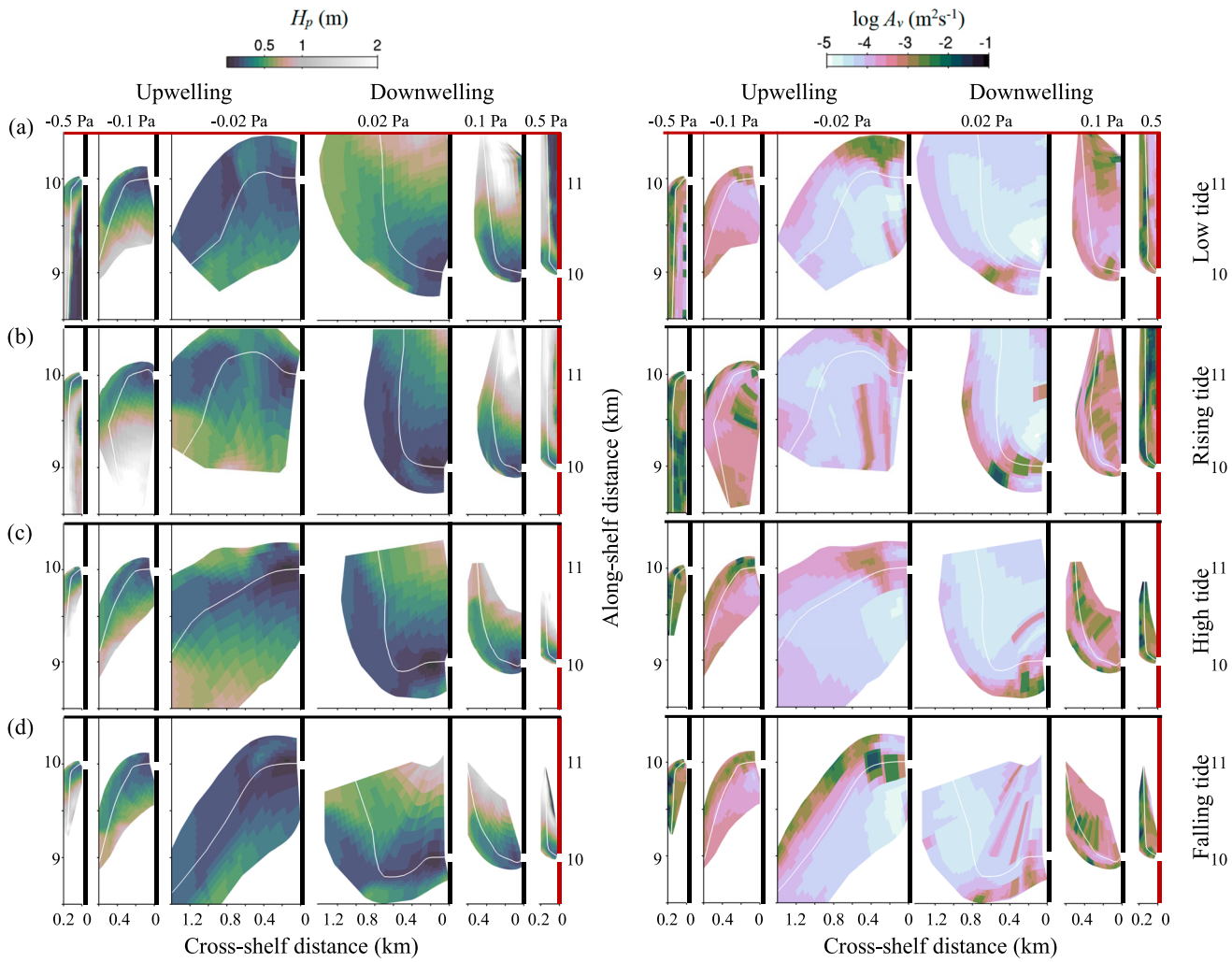

Figure A1. Snap-shots of the plume thickness (left panel) and the eddy viscosity coefficient at the plume base (right panel) for different wind scenarios and tidal phases.

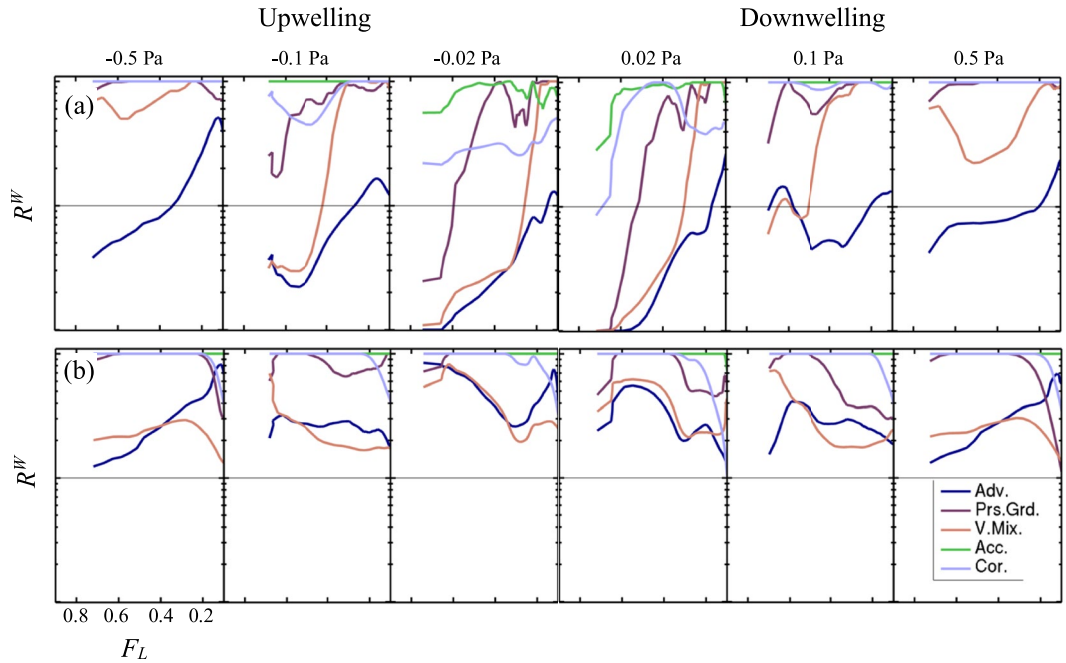

Figure A2. Ratio of the wind stress and the tidally averaged momentum terms $R^w = \left(\tau/\overline{\rho}_{pl} H_p\right)/Mom.$ with the plume layer averaged density $\overline{\rho}_{pl}$. Each momentum term that is, advection (*Adv.*), pressure gradient (*Prs.Grd.*), vertical mixing (*V.Mix.*), acceleration (*Acc.*), and Coriolis (*Cor.*) is shown in different color. The R^w is calculated in (a) along-plume and (b) cross-plume directions. The along-plume component is calculated along the centerline and averaged over the plume layer. The cross-plume component is calculated over the plume mesh (Figure 1c) and first averaged over the plume layer, then over the surface area. The mouth to tail plume distance is transformed to the tidally averaged outflow fraction rate. The horizontal line denotes $R^W = 1$; log-scale y-axis ranges from 0.1 to 10.

A2. Tide-Averaged Plume-Layer Dynamics

ROMS diagnostics were used to compute the tide-averaged momentum terms (*Mom.*) in along-plume and cross-plume directions (Basdurak et al., 2020). The dominant terms that is, advection (*Adv.*), pressure gradient (*Prs.Grd.*), vertical mixing (*V.Mix.*), acceleration (*Acc.*), and Coriolis (*Cor.*) were averaged over the plume-layer (Figure A2) to quantify the relative contribution of wind stress to each term with a dimensionless scale $R^w = \left(\tau/\overline{\rho}_{pl} H_p\right)/Mom.$ To compare the down-plume variation for each scenario, R^w is shown in terms of outflow fraction F (~0 at the plume-tail, Figure A2). The importance of wind stress on plume propagation enhances down-plume (Figure A2a). The deflection of the plume layer is driven by winds except when its diluted ($F < 0.2$), Coriolis and gradients associated with ambient currents take over; contribution of *V.Mix.* increases with wind strength (Figure A2b).

Data Availability Statement

The datasets used to produce the figures are openly available as Matlab files with variables described in a pdf file at http://doi.io-warnemuende.de/10.12754/data-2022-0009.

Acknowledgments
This study was funded by the National Science Foundation Project numbers (Evolution & Ecology of Infectious Diseases program; OCE-1065990) and the California Ocean Protection Council. Open access fees were covered by Leibniz Institute für Ostseeforschung Warnemünde through the ProjektDEAL. Open access funding enabled and organized by Projekt DEAL.

References

Basdurak, N. B., Largier, J. L., & Nidzieko, N. J. (2020). Modeling the dynamics of small-scale river and creek plumes in tidal waters. *Journal of Geophysical Research: Oceans*, *125*(7), e2019JC015737. https://doi.org/10.1029/2019jc015737

Clarke, L. B., Ackerman, D., & Largier, J. L. (2007). Dye dispersion in the surf zone: Measurements and simple models. *Continental Shelf Research*, *27*(5), 650–669. https://doi.org/10.1016/j.csr.2006.10.010

Fong, D. A., & Geyer, W. R. (2001). Response of a river plume during an upwelling favorable wind event. *Journal of Geophysical Research*, *106*(C1), 1067–1084. https://doi.org/10.1029/2000jc900134

Fong, D. A., & Geyer, W. R. (2002). The alongshore transport of freshwater in a surface-trapped river plume. *Journal of Physical Oceanography*, *32*(3), 957–972. https://doi.org/10.1175/1520-0485(2002)032<0957:tatofi>2.0.co;2

García Berdeal, I., Hickey, B. M., & Kawase, M. (2002). Influence of wind stress and ambient flow on a high discharge river plume. *Journal of Geophysical Research*, *107*(C9), 13–21. https://doi.org/10.1029/2001jc000932
Geyer, W. R., Hill, P., Milligan, T., & Traykovski, P. (2000). The structure of the Eel River plume during floods. *Continental Shelf Research*, *20*(16), 2067–2093. https://doi.org/10.1016/s0278-4343(00)00063-7
Hickey, B. M. S. L., Geier, S., Kachel, N., & MacFadyen, A. (2005). A bi-directional river plume: The Columbia in summer. *Continental Shelf Research*, *25*(14), 1631–1656. https://doi.org/10.1016/j.csr.2005.04.010
Jirka, G. H., Stolzenbach, K. D., & Adams, E. E. (1981). Buoyant surface jets. *Journal of the Hydraulics Division*, *107*(11), 1467–1487. https://doi.org/10.1061/jyceaj.0005764
Jurisa, J. T., & Chant, R. (2012). The coupled Hudson River estuarine-plume response to variable wind and river forcings. *Ocean Dynamics*, *62*(5), 771–784. https://doi.org/10.1007/s10236-012-0527-7
Kakoulaki, G., MacDonald, D., & Horner-Devine, A. R. (2014). The role of wind in the near field and midfield of a river plume. *Geophysical Research Letters*, *41*(14), 5132–5138. https://doi.org/10.1002/2014gl060606
Kastner, S. E., Horner-Devine, A. R., & Thomson, J. (2018). The influence of wind and waves on spreading and mixing in the Fraser River plume. *Journal of Geophysical Research: Oceans*, *123*(9), 6818–6840. https://doi.org/10.1029/2018jc013765
Kastner, S. E., Horner-Devine, A. R., & Thomson, J. M. (2019). A conceptual model of a river plume in the surf zone. *Journal of Geophysical Research: Oceans*, *124*(11), 8060–8078. https://doi.org/10.1029/2019jc015510
Kirincich, A. R., Barth, J. A., Grantham, B. A., Menge, B. A., & Lubchenco, J. (2005). Wind-driven inner-shelf circulation off central Oregon during summer. *Journal of Geophysical Research*, *110*(C10), C10S03. https://doi.org/10.1029/2004jc002611
Kirincich, A. R., Lentz, S. J., & Barth, J. A. (2009). Wave-driven inner-shelf motions on the Oregon coast. *Journal of Physical Oceanography*, *39*(11), 2942–2956. https://doi.org/10.1175/2009jpo4041.1
Kumar, N., & Feddersen, F. (2017). The effect of Stokes drift and transient rip currents on the inner shelf. Part II: With stratification. *Journal of Physical Oceanography*, *47*(1), 243–260. https://doi.org/10.1175/jpo-d-16-0077.1
Largier, J. L. (1992). Tidal intrusion fronts. *Estuaries*, *15*(1), 26–39. https://doi.org/10.2307/1352707
Lentz, S. J., & Largier, J. (2006). The influence of wind forcing on the Chesapeake Bay buoyant coastal current. *Journal of Physical Oceanography*, *36*(7), 1305–1316. https://doi.org/10.1175/jpo2909.1
McCabe, R. M., Hickey, B. M., & MacCready, P. (2008). Observational estimates of entrainment and vertical salt flux in the interior of a spreading river plume. *Journal of Geophysical Research: Oceans*, *113*(C8). https://doi.org/10.1029/2007JC004361
Moffat, C., & Lentz, S. (2012). On the response of a buoyant plume to downwelling-favorable wind stress. *Journal of Physical Oceanography*, *42*(7), 1083–1098. https://doi.org/10.1175/jpo-d-11-015.1
Nickols, K. J., Gaylord, B., & Largier, J. L. (2012). The coastal boundary layer: Predictable current structure decreases alongshore transport and alters scales of dispersal. *Marine Ecology Progress Series*, *464*, 17–35. https://doi.org/10.3354/meps09875
Osadchiev, A., & Sedakov, R. (2019). Spreading dynamics of small river plumes off the northeastern coast of the Black Sea observed by Landsat 8 and Sentinel-2. *Remote Sensing of Environment*, *221*, 522–533. https://doi.org/10.1016/j.rse.2018.11.043
Pimenta, F. M., & Kirwan, A. D., Jr. (2014). The response of large outflows to wind forcing. *Continental Shelf Research*, *89*, 24–37. https://doi.org/10.1016/j.csr.2013.11.006
Pullen, J. D., & Allen, J. S. (2000). Modeling studies of the coastal circulation off northern California: Shelf response to a major Eel river flood event. *Continental Shelf Research*, *20*(16), 2213–2238. https://doi.org/10.1016/s0278-4343(00)00068-6
Rennie, S. E., Largier, J. L., & Lentz, S. J. (1999). Observations of a pulsed buoyancy current downstream of Chesapeake Bay. *Journal of Geophysical Research*, *104*(C8), 18227–18240. https://doi.org/10.1029/1999jc900153
Rijnsburger, S., Flores, R. P., Pietrzak, J. D., Horner-Devine, A. R., & Souza, A. J. (2018). The influence of tide and wind on the propagation of fronts in a shallow river plume. *Journal of Geophysical Research: Oceans*, *123*(8), 5426–5442. https://doi.org/10.1029/2017jc013422
Rodriguez, A. R., Giddings, S. N., & Kumar, N. (2018). Impacts of nearshore wave-current interaction on transport and mixing of small-scale buoyant plumes. *Geophysical Research Letters*, *45*(16), 8379–8389. https://doi.org/10.1029/2018gl078328
Salcedo-Castro, J., Saldías, G. S., Saavedra, F., & Donoso, D. (2020). Climatology of Maipo and Rapel river plumes off Central Chile from numerical simulations. *Regional Studies in Marine Science*, *38*, 101389. https://doi.org/10.1016/j.rsma.2020.101389
Tilburg, C. E., Gill, S. M., Zeeman, S. I., Carlson, A. E., Arienti, T. W., Eickhorst, J. A., & Yund, P. O. (2011). Characteristics of a shallow river plume: Observations from the Saco river coastal observing system. *Estuaries and Coasts*, *34*(4), 785–799. https://doi.org/10.1007/s12237-011-9401-y
Warrick, J. A., & Farnsworth, K. L. (2017). Coastal river plumes: Collisions and coalescence. *Progress in Oceanography*, *151*, 245–260. https://doi.org/10.1016/j.pocean.2016.11.008
Whitney, M. M., & Garvine, R. W. (2005). Wind influence on a coastal buoyant outflow. *Journal of Geophysical Research: Oceans*, *110*(C3). https://doi.org/10.1029/2003JC002261
Wong, S. H., Monismith, S. G., & Boehm, A. B. (2013). Simple estimate of entrainment rate of pollutants from a coastal discharge into the surf zone. *Environmental Science & Technology*, *47*(20), 11554–11561. https://doi.org/10.1021/es402492f
Zhao, J., Gong, W., & Shen, J. (2018). The effect of wind on the dispersal of a tropical small river plume. *Frontiers of Earth Science*, *12*(1), 170–190.

Erratum

In the originally published version of this article, the caption for Figure 3 contained typographical errors. In the first sentence, "currents" has been updated to "currents V" and "(f)" has been updated to "F." In addition, the following text has been added to the end of the caption of Figure A2: The horizontal line denotes $R^W = 1$; log-scale y-axis ranges from 0.1 to 10. The corrections have been made, and this may be considered the authoritative version of record.